NASA CONTRACTOR REPORT

NASA CR-1573

AN EXPERIMENTAL STUDY OF ROTOR BLADE-VORTEX INTERACTION

by Makam Surendraiah

Prepared by
THE PENNSYLVANIA STATE UNIVERSITY
University Park, Pa.
for Langley Research Center

NATIONAL AERONAUTICS AND SPACE ADMINISTRATION • WASHINGTON, D. C. • MAY 1970

NASA CR-1573

~~AN~~ EXPERIMENTAL STUDY OF ROTOR BLADE-VORTEX INTERACTION*

By Makam Surendraiah

note : Thesis.

*Submitted in partial fulfillment of the requirements for the Degree of Master of Science, December 1969

May 70

Prepared under Grant No. NGR omit 39-009-111 by
M.E., ~~THE~~ PENNSYLVANIA STATE UNIVERSITY
University Park, Pa.

for Langley Research Center

NATIONAL AERONAUTICS AND SPACE ADMINISTRATION

For sale by the Clearinghouse for Federal Scientific and Technical Information
Springfield, Virginia 22151 – CFSTI price $3.00

ABSTRACT

Results of an experimental investigation of the instantaneous blade airloads and their time derivatives are presented for a rotor blade intersecting a completely rolled up trailing vortex. Parameters such as the rotor RPM, vortex strength, and intersection angle were examined at a spanwise station of 0.95R.

An unsteady section lift coefficient value as high as 0.7 and its time derivative, 0.6×10^3/sec, were measured during the vortex sweep. The values were found to decrease with radial distance from the center of the vortex. The commonly heard helicopter blade slap or bang was clearly heard in the present tests. Test results indicated vortex interaction is negligible for rotor plane positions beyond approximately one and one-half blade chord lengths from the vortex center.

The rotor blade experienced as much negative lift as positive lift during its encounter with the tip vortex. Sample photographic records are presented in order to show the influence of the tip vortex on the blade loading.

ACKNOWLEDGMENTS

The author wishes to extend his gratitude to his advisor, Professor Barnes W. McCormick, for his advice and encouragement during the preparation of this thesis. The writer also thanks Mr. Gerald F. Hall for his general comments and discussions.

The research contained in this thesis was sponsored by the National Aeronautics and Space Administration (Langley) Contract No. NGR 39-009-111, and is gratefully acknowledged.

Table of Contents

NOMENCLATURE

c	Blade chord
R	Blade radius
C_w	Vortex-generated wing chord
r	Radius at any spanwise station from center of rotation. Also running variable radial distance from the center of the vortex.
Z	Distance between rotor axis and vortex axis, defined in Fig. 2.
h	Radial distance from the center of the vortex, defined in Fig. 1.
V	Free stream velocity
v_θ	Tangential velocity
V_r	Blade velocity at spanwise station r, $= \omega r$
V_T	Blade tip velocity
L	Load/span
C_ℓ	Section lift coefficient, $L/\frac{1}{2}\rho V_r^2 c$
ΔC_ℓ	Maximum section lift coefficient difference in any vortex sweep, defined in Fig. 13
Δt	Impulsive time, defined in Fig. 13.
$\Delta\alpha$	Maximum angle of attack change of rotor blade in any vortex sweep.
ζ	Vorticity at any radius
ζ_o	Vorticity at center of vortex
w	Width of vortex at which $\zeta = \frac{\zeta_o}{2}$
a	Core radius (radius where $v_\theta(r)$ is a maximum)
Γ	Circulation at any radius
$\Gamma(a)$	Circulation at the radius 'a' for maximum v_θ.

ΔP Pressure difference at a chordwise station

C_P Differential pressure coefficient; $\frac{\Delta P}{\frac{1}{2}\rho V_T^2}$

δ Intersection angle, defined in Fig. 2.

H Downstream distance from vortex-generated wing trailing edge.

α_w Vortex-generated wing angle of attack.

α Sectional angle of attack of rotor blade.

LIST OF TABLES

LIST OF FIGURES

I. INTRODUCTION

A lifting rotor, either while hovering or moving through a fluid, produces a differential pressure field across the rotor plane in order to support its weight and provide thrust for its forward movement. It also leaves behind a continuous vortex sheet because of the lift variation along the span of the blade. This vortex sheet rolls up rapidly into two distinct vortices, one at the tip and the other at the hub.

The diffuse inboard vortex sheet tends to be dissipated by viscosity more rapidly than the stronger outboard sheet which rolls up into the tip vortex. On a single-bladed configuration, if roll-up occurs, this diffuse inboard sheet will form a hub vortex with a larger core and smaller induced velocities than the tip vortex. However, on a multi-bladed configuration, the relatively weak hub vortices from the several blades will combine to form a single hub vortex which is stronger than the individual tip vortices. But this hub vortex is carried down and aft from the rotor by the inflow and free-stream and so is relatively far removed from the blade paths. Hence blade intersection with this vortex will, in general, not occur and we need only consider the intersection with tip vortex.

The maximum tangential velocity induced by a tip vortex can be as high as 47% of the free stream velocity[16]. A following blade can intersect a tip vortex from a preceding blade and experience momentarily a sudden change in velocity or a sudden change in angle of attack or both, depending on the vortex orientation relative to the

blade direction. These events are shown schematically in Fig. 1. These events occurring on the following blade give rise to a sudden impulse or load variation over a small spanwise distance and in a short interval of time. In total, what we experience, the structural vibrations and a sharp cracking sound known as blade slap or bang, is a result of this impulsive load[4]. The magnitude of this impulsive load varies with changes in both the intersection point and the angle δ. This angle, shown in Fig. 2, is the angle between the vortex axis and the blade direction. It was shown in reference 13 that the effect of the vortex will be larger for small values of δ than for values near 90°.

Because of the skewed character of the wake system during forward flight, there is a non-uniform distribution of induced velocity over the rotor disc which gives rise to harmonic loads acting on the blades. Most of these variations are attributed to the strong tip trailing vortices. This has been shown theoretically by Miller[9,10] and Piziali et al.[12] and experimentally by Scheiman and Ludi[14].

In most theoretical considerations (References 9,17,18) the wake system has been divided into two sections, namely, the "near" wake and the "far" wake. The near wake is approximately the first 90° of the wake attached to the blade and is comprised of all elements of shed and trailing vorticity. The far wake is the remainder of the wake system and is comprised of root and tip trailing vortices. Assuming the spiral vortex lines to be replaced by infinite straight vortex lines, Miller[11] provides a simple method for calculating the effect of the far wake. However for the near wake, numerical methods have been

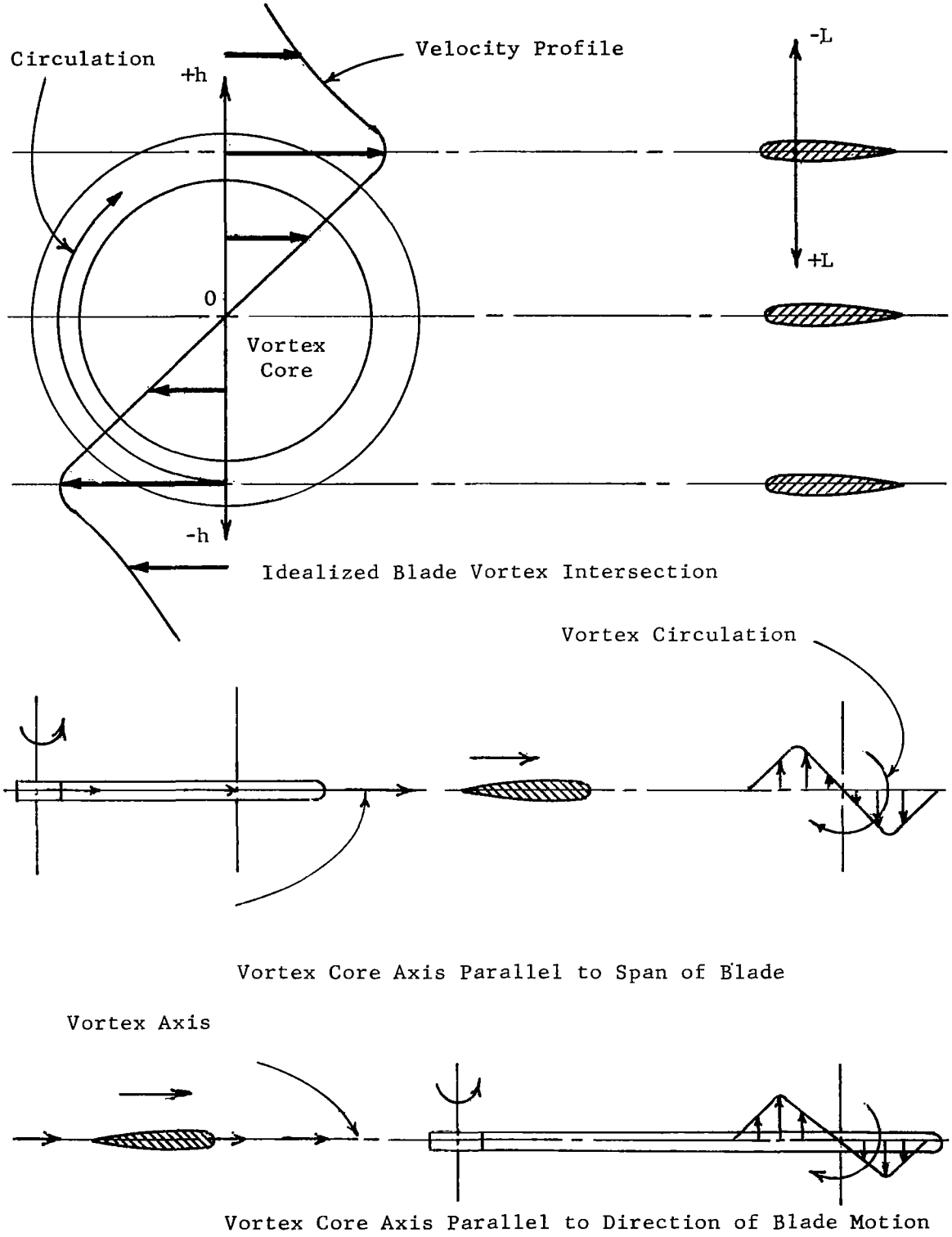

Fig. 1 Blade Vortex Intersections

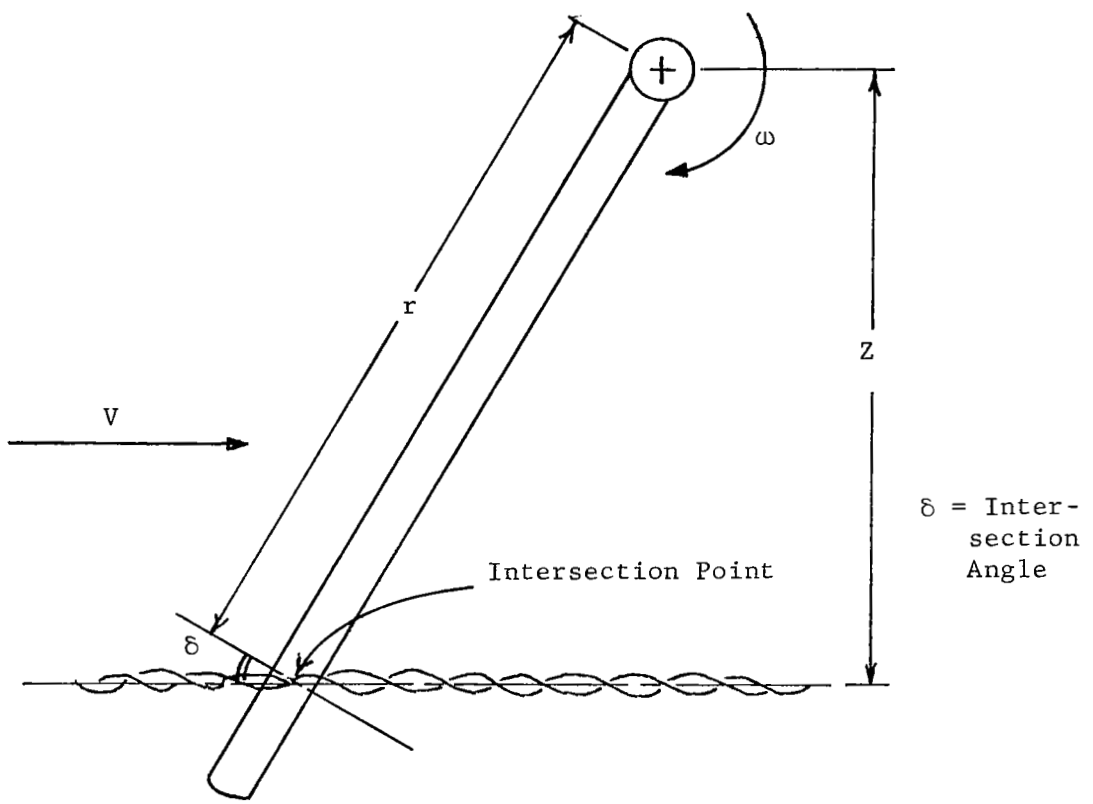

Fig. 2 Sketch of Blade Passing Through a Tip Vortex

used[9,12]. Willmer[18] has used an extension of classical lifting line theory to take into account the trailing components.

Previous analysis, such as those cited, have been primarily concerned with unsteady lift as affected by an entire wake under the assumption of potential flow. Little attention has been paid to the details of the interaction between a blade and isolated vortex in terms of expected blade aerodynamic response and possible real fluid effects. Such description requires a knowledge of the unsteady pressure field associated with the interaction.

This investigation is concerned only with the rotor-isolated vortex interaction problem. The rotor blade is a symmetrical airfoil at zero pitch angle. The rotor disc plane is also at a zero angle of attack. The rotor blade intersects a completely rolled up vortex generated by a fixed wing ahead of the rotor plane. The time history of the chordwise pressure distribution is recorded. The principal variables in this experiment are the rotor RPM, vortex structure and strength, rotor plane position and angle of intersection.

II. PREVIOUS INVESTIGATIONS

Time-dependent spanwise and chordwise pressure distributions have been measured on full-scale helicopter rotors using conventional differential transducers[1,3,8,14]. However these transducers may experience a time lag in their pressure measurements because of the connecting tube. In addition, they also have a lower frequency response than the transducers used here.

A similar type of investigation was done at Southampton University[5] in connection with helicopter blade slap. In that investigation, a simulated tip vortex was generated by means of two air jets mounted slightly offset in opposite directions. The maximum induced angle or induced velocity obtained from the above method is only 75% of that of an actual tip vortex[7]. Measurements were made of sound pressure levels rather than detailed pressure measurements.

In a paper by Simons[15], the problem of blade/vortex interaction on rotors was dealt with theoretically using lifting line theory for the computation of circulation distribution along a wing span for various locations of the vortex line with respect to the wing and also for different vortex core radii. The effect of blade-vortex intersection is described by two parameters, the effective height and strength factor. The effective height is just the actual height of the vortex from the wing plus one-half of the blade chord. The effective strength factor is the ratio of the maximum wing bound circulation, including the effects of the intersecting vortex, to the strength of the intersecting vortex. However, for vortex heights less

than three-quarters of a chord this concept becomes increasingly inaccurate. Simons thus suggests a more realistic blade/vortex general investigation is required before these concepts can be applied directly to the helicopter rotor.

Significant airload pressure variations due to rotor tip vortex interference have been measured in flight[13]. Section pressures were considerably different from those of a two-dimensional airfoil over significant areas of the rotor disc, apparently due to the combined effects of compressibility and the disturbances from tip vortex interference. The local Mach number can reach the critical Mach number especially near the tip of the advancing blade. This can separate the boundary layer, thereby causing a change in the chordwise pressure distribution. A typical response of the chordwise pressure distribution to the vortex interference spike for the aft rotor, taken from Fig. 7 of the cited reference, is shown in Fig. 3. It was also noticed that it requires about 50° of azimuth travel before the blade section performance returns to a two-dimensional character.

Scheiman and Ludi[14] also observed the tip vortex interference on the following blade in a free flight investigation. The main differences between their measured results and the results from uniform inflow theory were shown to occur near the intersection of the blade with the trailing vortices of the preceding blade. In addition, the influence of the trailing vortices produce harmonic blade loadings of all orders, and the percentage of the contribution to the higher harmonics is large.

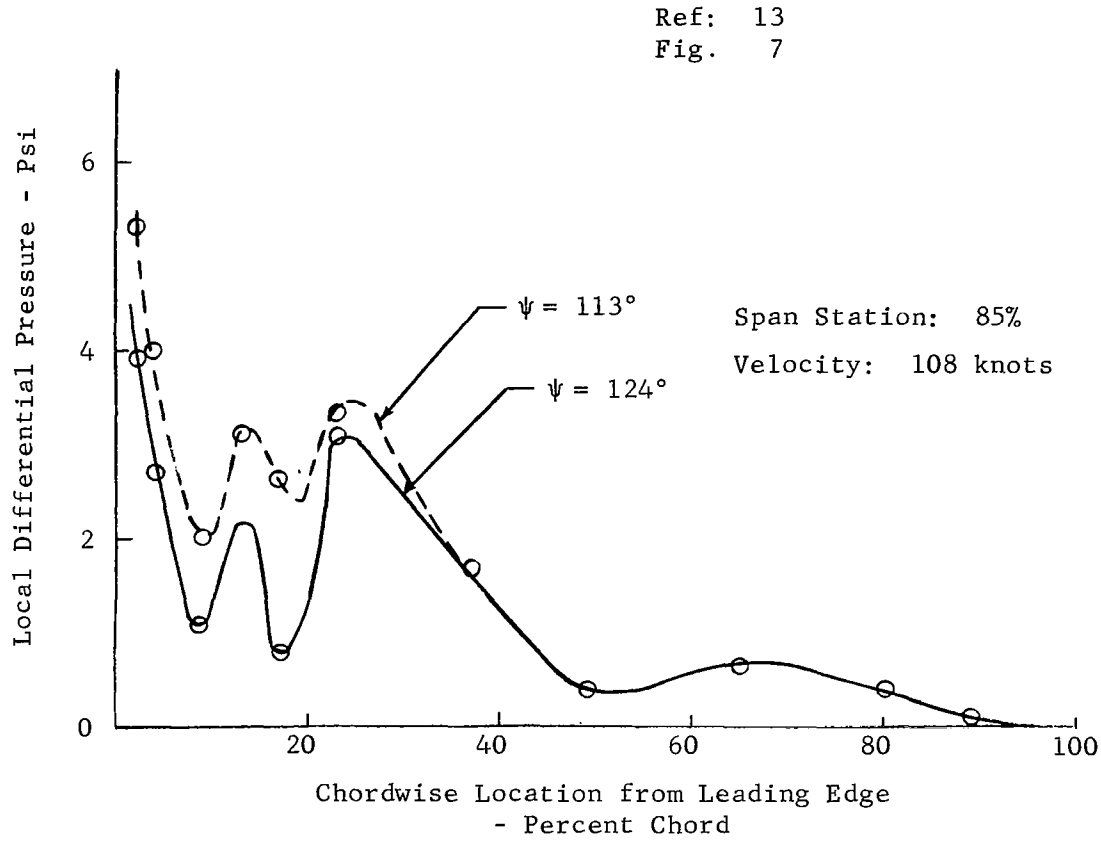

Fig. 3 Typical Chordwise Pressure Distributions of Aft Rotor in Proximity of Forward Rotor Tip Vortex

III. DESCRIPTION OF EXPERIMENTAL SET-UP

The experimental set-up used in the present investigation is shown in Fig. 4a. It primarily consists of a heavy structure made up of 'L' sections in order to make it rigid and free from oscillations. A rigid, horizontal base was attached to it. Adjustment was provided for the base to be positioned vertically and horizontally so that the blade could intersect the vortex system at different orientations. A thick-walled hollow shaft was mounted on the base by means of two pillow blocks. On one end of the shaft, a single, instrumented blade was fixed with the other end coupled to a twelve channel slip ring unit. The blade was counterblanced by using a lead sphere fixed on a threaded rod. The diameter of the sphere was chosen from a consideration of the centrifugal force and wake size. For normal operation it is located at a radius equal to half of the blade radius. An ellipsoidal body of revolution was used for the nose fairing. The shaft was driven by a 3/4 H.P. variable speed motor mounted underneath the base plate using a belt system.

Rotor Blade

A single bladed rotor system was used for the tests. This was adopted in order to eliminate the tip and wake effects of the other blades. It was also shown in reference (1) that the removal of one blade from a two bladed rotor system, no serious differences resulted in loading, total lift variation, or inflow distribution.

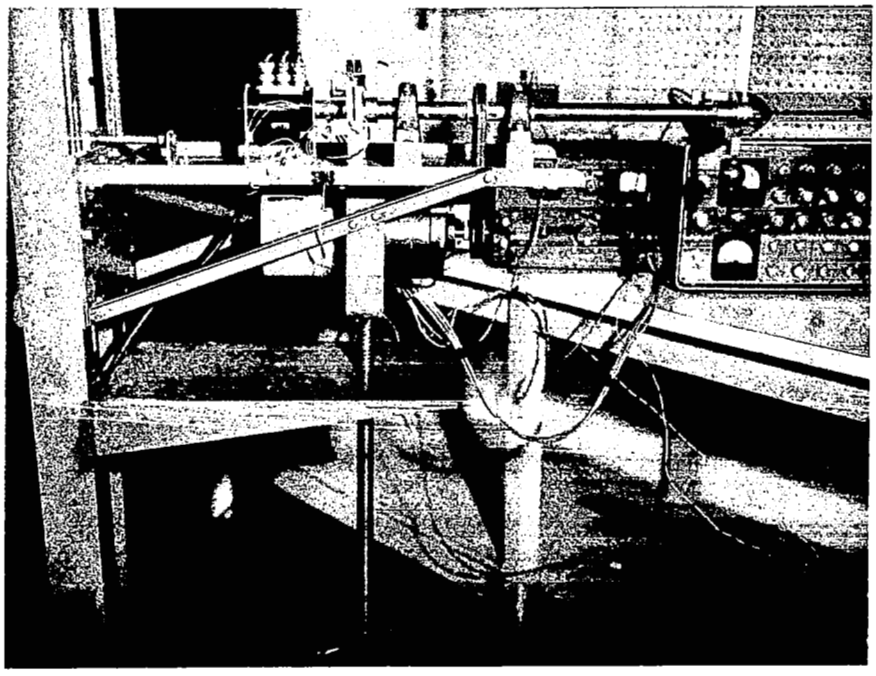

Fig. 4a Experimental Set-Up

The rotor blade dimensions were dictated mainly by the testing facilities available and the desire to obtain reasonable data for comparison with theory. The blade was one foot in radius and two inches in chord having a NACA 0015 airfoil section made of high strength aluminum (Figs. 4b and 4c). The tip was a revolution of the blade section. Grooves of sufficient size and depth to accommodate the miniature pressure sensors were made on one surface of the blade at four spanwise stations; 0.95R, 0.90R, 0.85R and 0.75R. The electrical lead wires followed along the spanwise groove on the blade through the shaft to the slip ring unit. The overall stiffness EI of the blade was 0.01585×10^6 lbs in^2 and the mass distribution M was 0.0013 slugs/in.

Vortex Generation and Measurements

The experiments were conducted in the subsonic wind-tunnel of the Department of Aerospace Engineering at The Pennsylvania State University. The tunnel was run with an open jet test section, such that the rotor could be moved up and down. A bell-mouth entrance section was used for smooth re-entry of air into the diffuser. Pressure surveys were conducted at two downstream distances in both horizontal and vertical directions in order to check for flow uniformity. It was found that the flow was uniform within 2% variation.

A 6" chord wing having the same aspect ratio and airfoil geometry of the rotor blade (Fig. 4c) was mounted vertically at the end of the contraction section for the generation of a vortex system. Vortex measurements were made for wing angles of 6° and 10°.

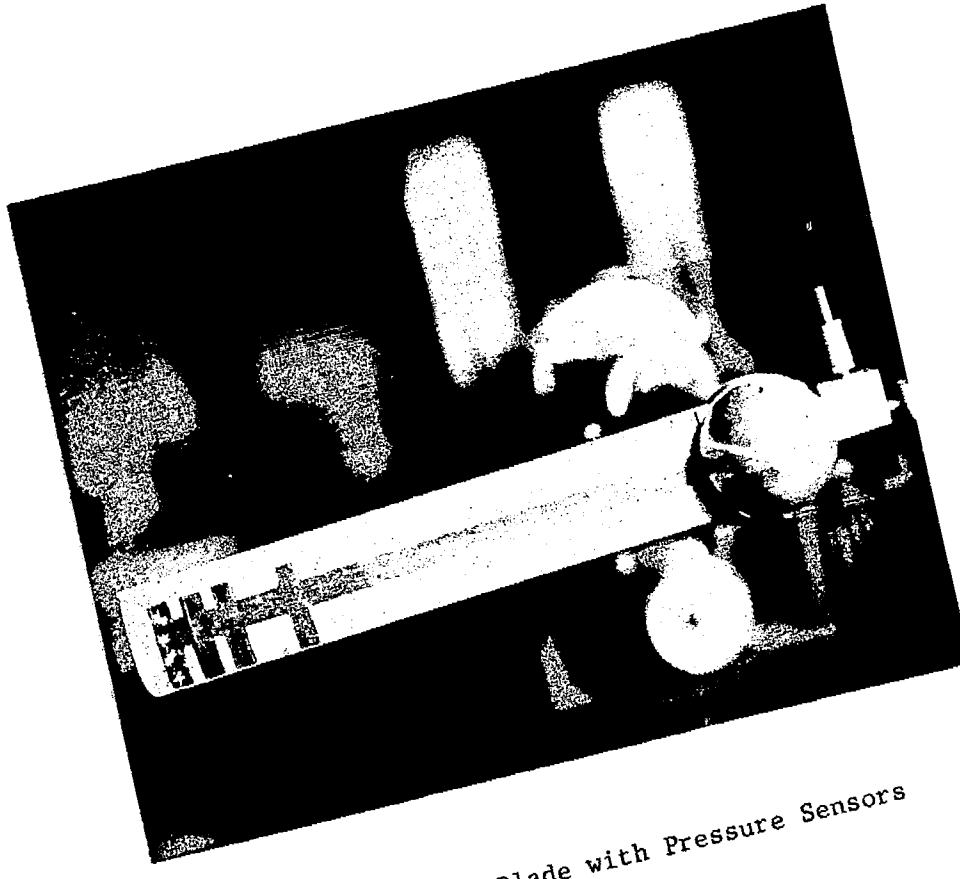

Fig. 4b Rotor Blade with Pressure Sensors

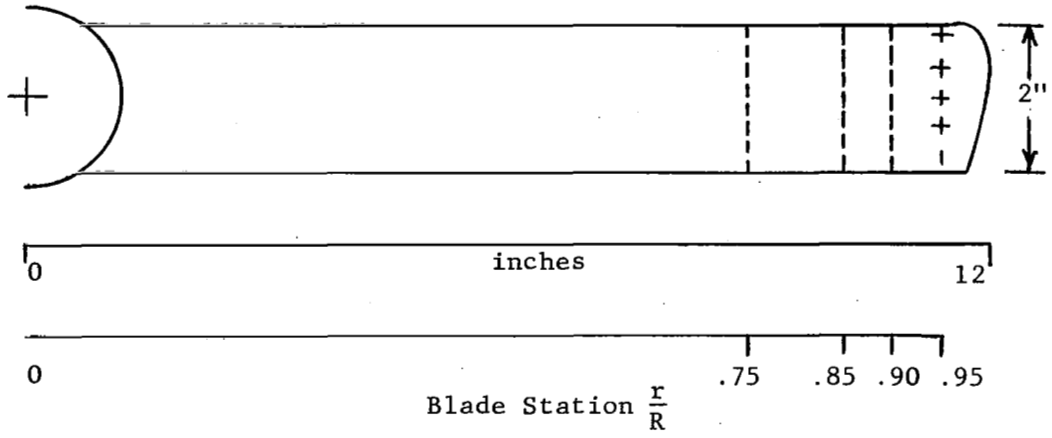

Pressure Sensor No.	x/c at r/R	0.95
1		0.0625
2		0.2875
3		0.4875
4		0.6875

NACA 0015

Rotor Blade; Pressure Sensor Locations

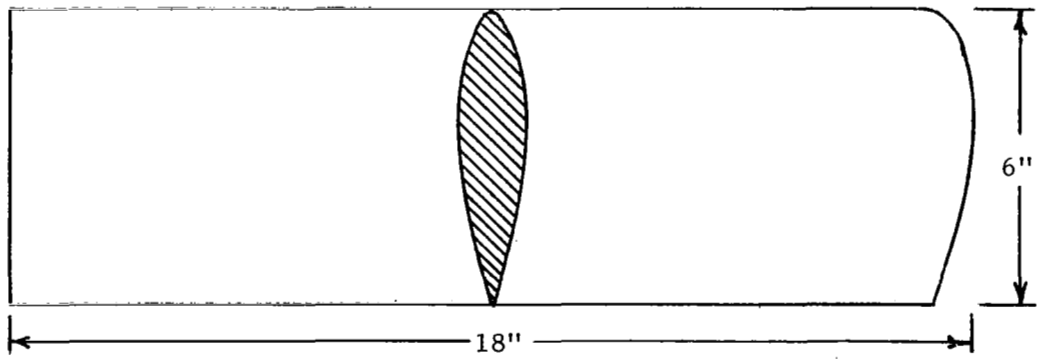

Fig. 4c Rotor Blade and Wing Details

Measurements were made using the vorticity meter developed by May[6]. This meter consists of four unpitched steel vanes mounted on an aluminum spinner. As the shaft rotates, a hole drilled through the shaft allows passage of light from a miniature light bulb to a photovoltaic cell. Two pulses of light pass through the hole for each revolution. These pulses are counted electronically as counts per second which are used as a measure of the vorticity. A typical vorticity distribution in the rolled-up tip vortex is shown in Fig. 5. Contours of constant rotational speeds are shown in Fig. 6 at a transverse plane of 3 chord lengths downstream. Measurements were also taken at a downstream distance of 5 chord lengths. These distances approximately locate the rotor position and rotor blade during its rotation.

The tangential velocity in a vortex can be obtained by numerically integrating the vorticity. Since the vortex was axisymmetric, as seen from contour plot (Fig. 6) the tangential velocity $v_\theta(r)$ at any radius r is

$$v_\theta(r) = \frac{1}{r} \int_0^r h\, \zeta dh \qquad (3.1)$$

where ζ is vorticity at any radius h, radians/sec. A calibration coefficient of 0.80, taken from reference 16 was used in the calculation of tangential velocity in order to take into account the frictional and windage losses. Figure 7 shows the variation of tangential velocity with the vortex radius for the 6° and 10° wing angles. The maximum tangential velocity obtained for the 10° case is nearly 46% of the free stream velocity. This is in general agreement with Spencer et al.[16].

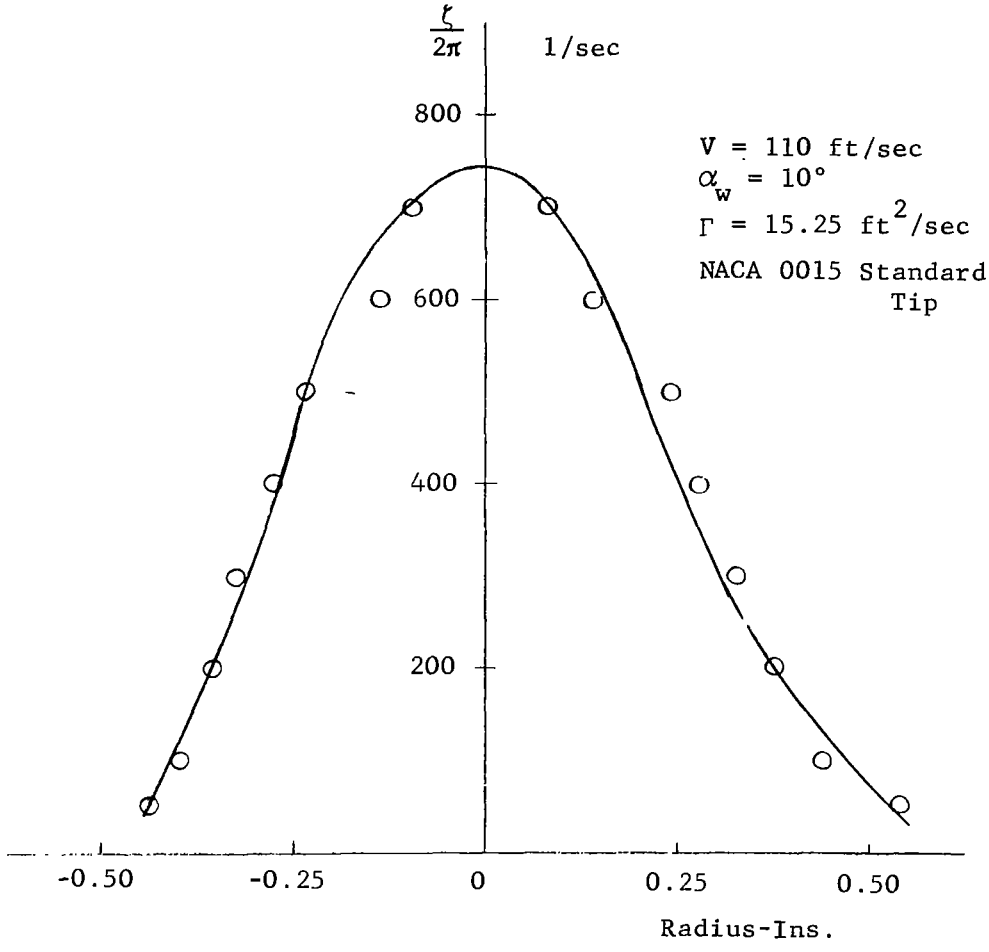

Fig. 5 Typical Vorticity Distribution

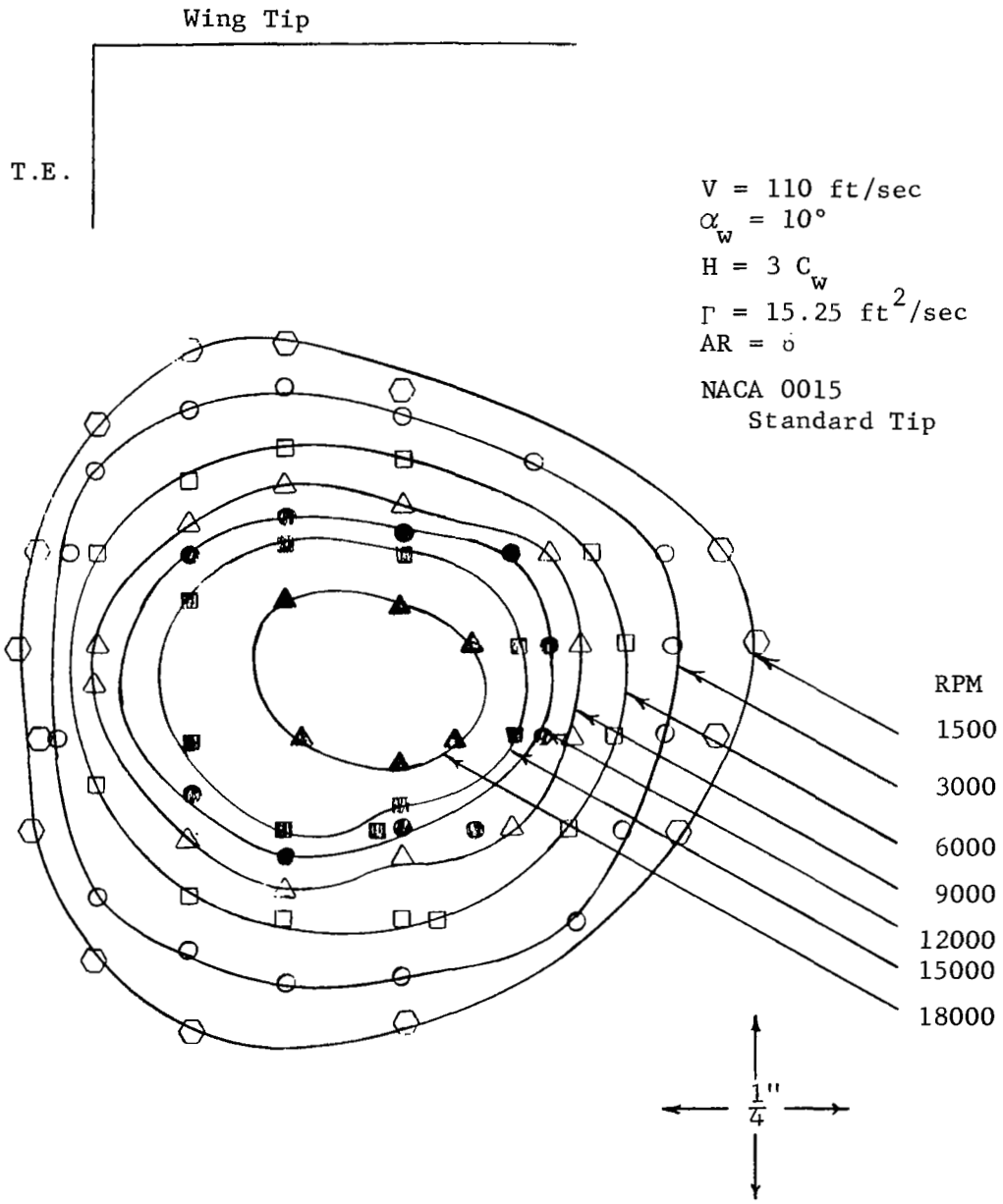

Fig. 6 Contours of Constant Rotational Speed

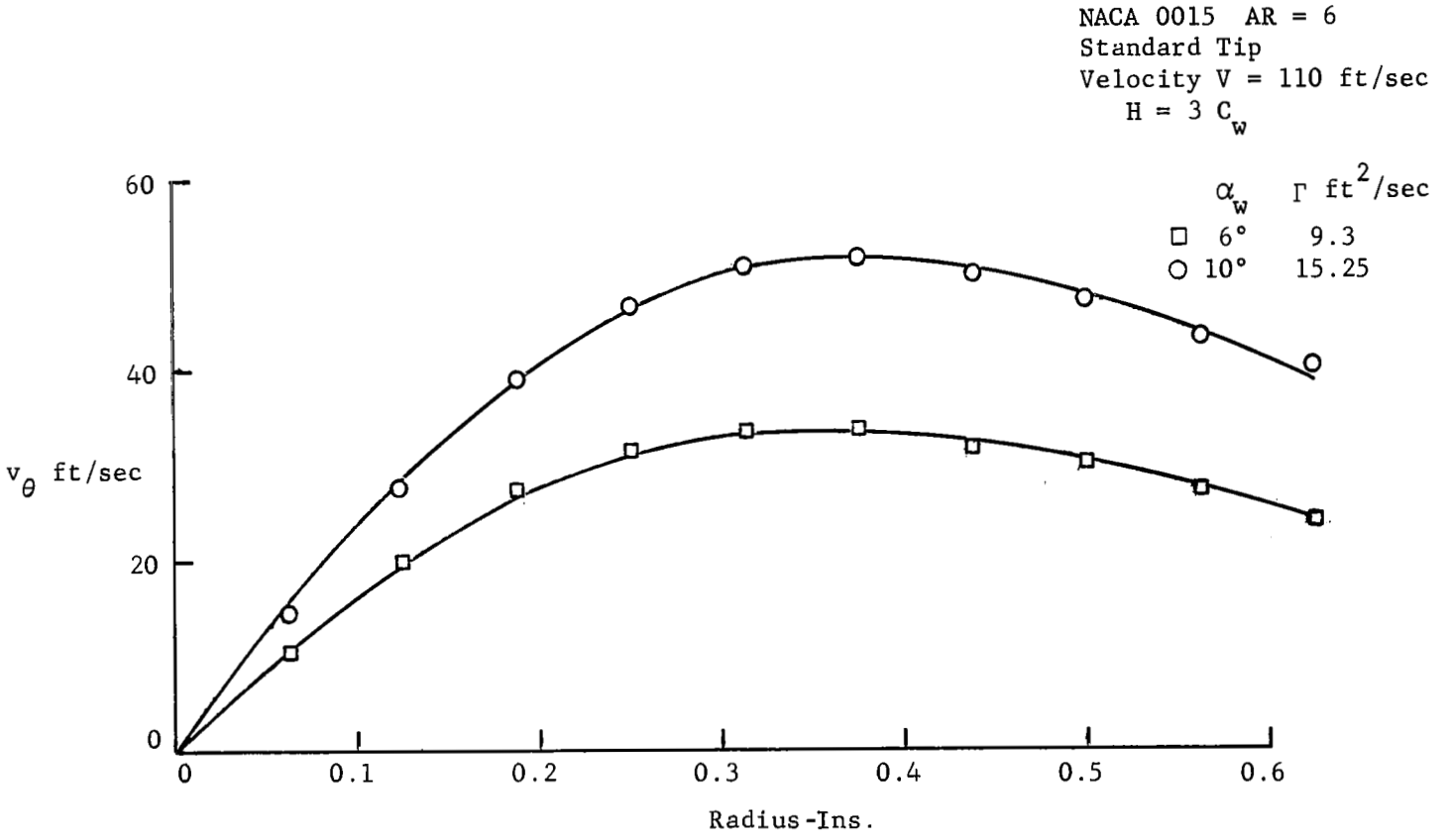

Fig. 7 Tangential Velocity Distribution
Through the Trailing Vortex

The circulatory strength of the vortex is obtained by numerically integrating the vorticity.

$$\Gamma = \int_{o}^{\infty} 2 \pi h \zeta dh \tag{3.2}$$

and, using an exponential fit, the vorticity distribution through the vortex core is of the form

$$\zeta = \zeta_o e^{-(\frac{h}{w})^2 \log_e 2} \tag{3.3}$$

where ζ_o is the maximum vorticity and w is the value of h for which $\zeta = \zeta_o / 2.0$. The circulation equation results in

$$\Gamma = \frac{\pi w^2}{\log_e 2} \zeta_o \tag{3.4}$$

The circulatory strength of the vortex for the two angles, 6° and 10° were 9.30 ft^2/sec and 15.25 ft^2/sec respectively, in agreement with reference (16). The core widths were 0.24" and 0.26" and maximum vorticities were 3425/sec and 4710/sec respectively.

Similar measurements and calculations were also made for the same negative angles of the wing and it was found that the vortex structure and velocity variations were the same as previously obtained. This was necessary because the rotor blade is instrumented on one surface only. To get the pressure distribution on the other surface, the direction of the vortex rotation is changed by changing the angle of the wing from a positive to a negative angle.

Pressure Measuring Equipment

The pressure transducers used in this experiment were ultra miniature pressure sensors made by Kulite Semiconductor Products Inc.

Each is made by using a monolithic integrated circuit Wheatstone bridge directly formed on a Silicon diaphragm. They are 1/8" in diameter and 0.002" thick with a natural frequency of 40 kc and a sensitivity of approximately 0.75 mv/v/psi. These sensors have a range of 0-25 psi.

All gauges were statically calibrated for linearity and sensitivity. A typical calibration curve is shown in Figs. 8a and 8b, one for low and the other for high pressure ranges. The output varies linearly with pressure, passing through zero, independent of excitation voltage within the range prescribed. The sensitivity varied in the range from 0.6 to 0.8 mv/v/psi for different pressure sensors. The temperature sensitivity of the gauges was less than 2%/100°F of full scale output. This effect was partially reduced by running the blade in the flow for a sufficient period of time before any measurements were made. By using this method, the blade reaches a stable temperature and any differences noticed are due to vortex interaction with the blade.

After calibration, these sensors were cemented by means of Eastman Kodak 910 adhesive on the blade groove at the required spanwise and chordwise locations. Nitro-methane solvent dissolves the adhesive, permitting the same sensors to be used at various spanwise stations.

Power Supply and Bridge Balancing Unit

As specified by Kulite, the gauges can be excited by 0-10 volts D.C. or A.C. RMS, or 0-10 Ma. constant current. Most of the tests were conducted at 6 V D.C.

A six-channel universal bridge balance unit Heiland "82-6", which serves as both a power supply and balancing unit, was used. The

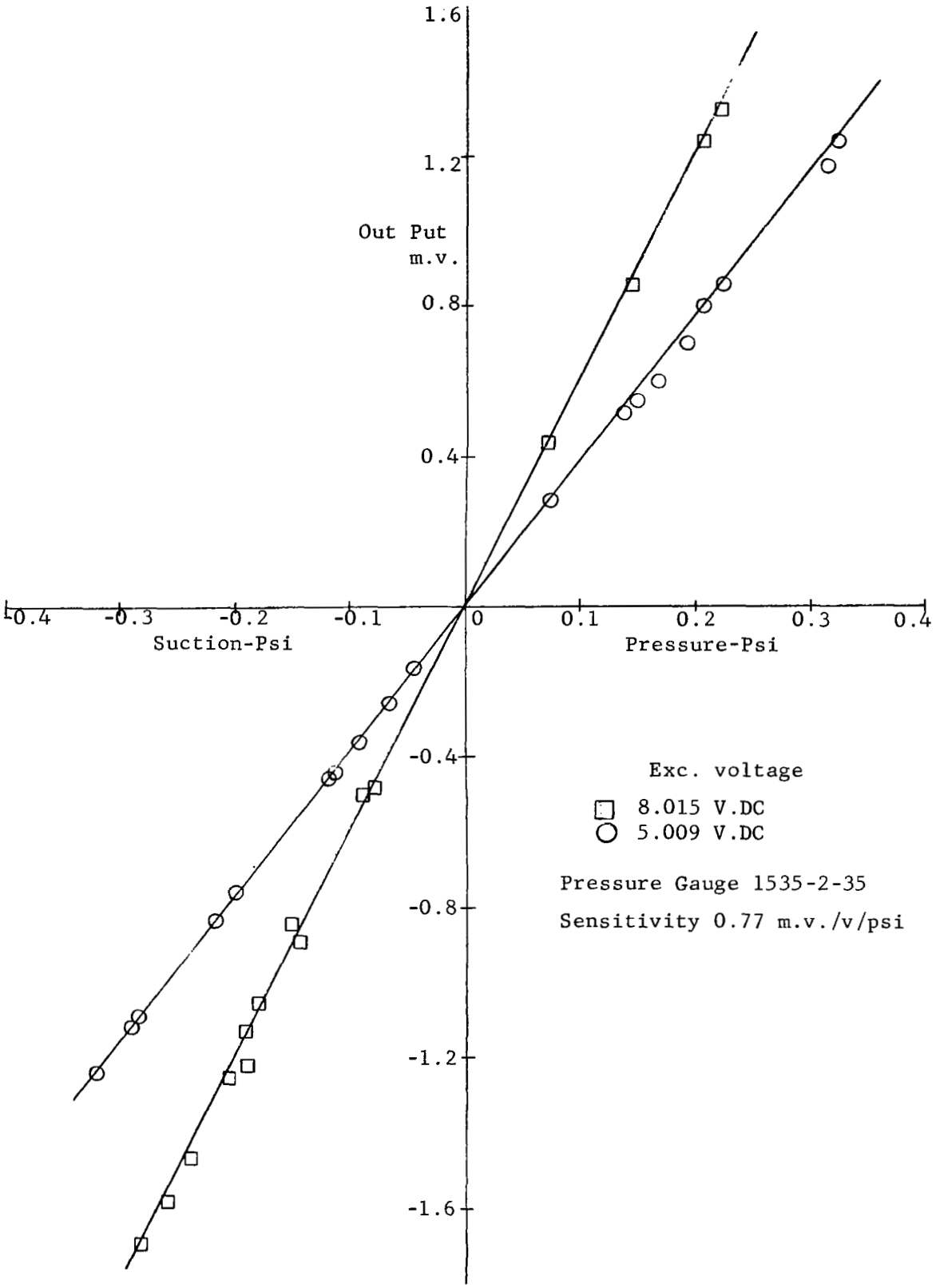

Fig. 8a Pressure Sensor Calibration
Low-Pressure Range

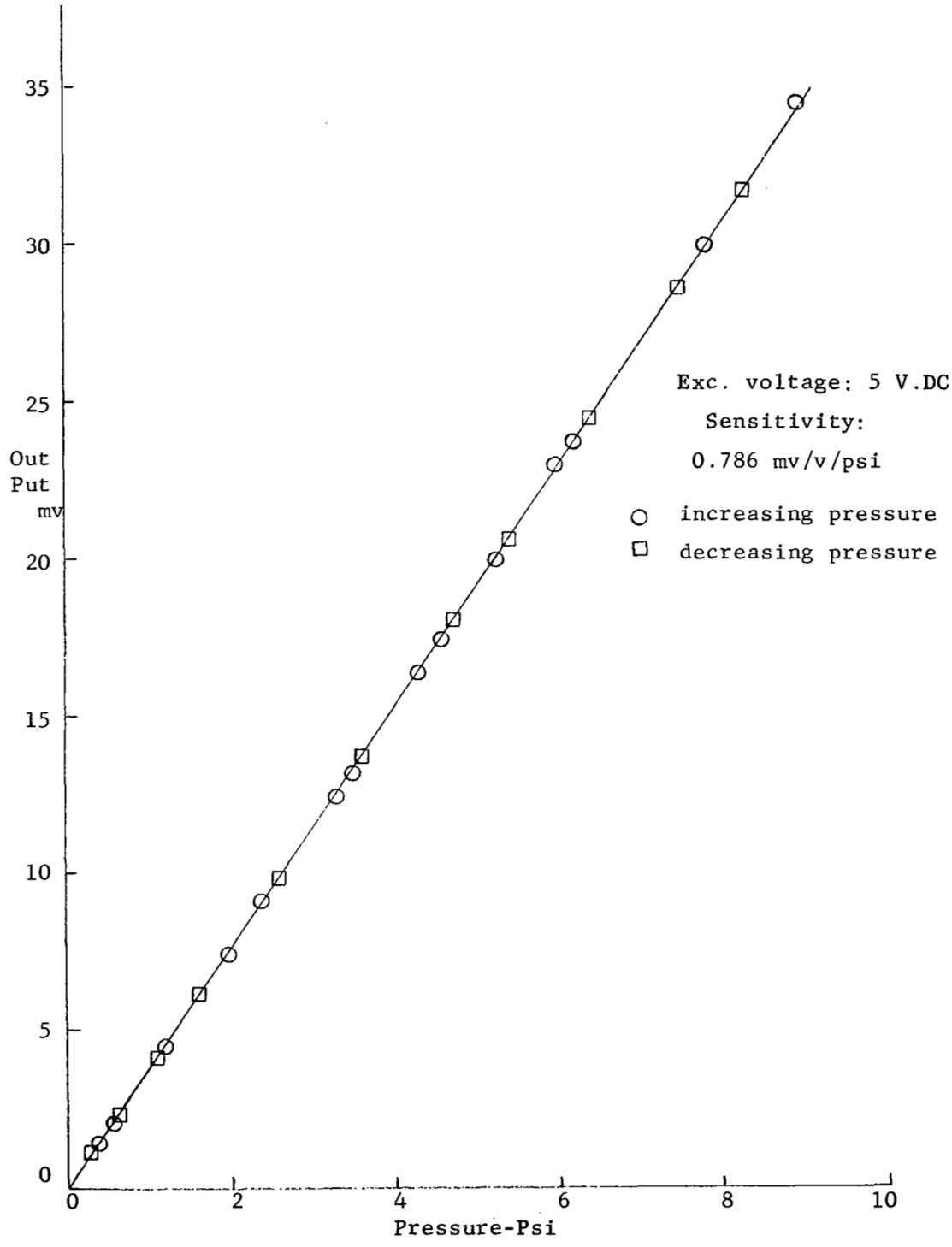

Fig. 8b Pressure Sensor Calibration
High Pressure Range

gauge inputs were connected in parallel and were brought out through the slip ring unit using only two rings. They were again connected in parallel to the balancing unit. The input voltage to the gauges was set by means of the coarse and fine voltage adjustment. The gauge outputs were brought out individually through the slip ring unit and connected to the bridge balance unit. The outputs from the balancing unit were fed to an oscilloscope through a channel selection switch and a common D.C. amplifier, Type 3520 DANA.

Balancing was done by first observing the transducer output meter followed by the scope. The experiments were conducted at a gain of 1000 and a band width of 1 kc. This can include all higher harmonics of load fluctuations. A block diagram of the wiring is shown in Fig. 9.

Counting and Triggering Mechanism

As mentioned previously, the rotor was rotated using a commercial variable speed motor and a pulley and belt system (Fig. 4a). The pulley diameters used were in 1:1 ratio and thus the speed of the motor indicates the speed of the rotor except for the play in the belt. To obtain the correct RPM of the rotor, a thin, circular disc was mounted on the shaft as shown in Fig. 10. Thirty equally spaced 1/8" diameter holes were drilled along the circumference of the disc. A semicircular slotted arch was then fixed over the disc. A light source (2.2 V Bulb) and photo cell were fixed on a U-section which was then mounted on the arch such that it aligned with the holes on the disc. The output from the photo cell, which were approximately 2 V D.C. pulses were fed to an electronic counter similar to the one used in vortex measurements. The RPM of the shaft was $\frac{\text{counts/sec}}{30} \times 60 = 2 \times \text{counts/sec}$.

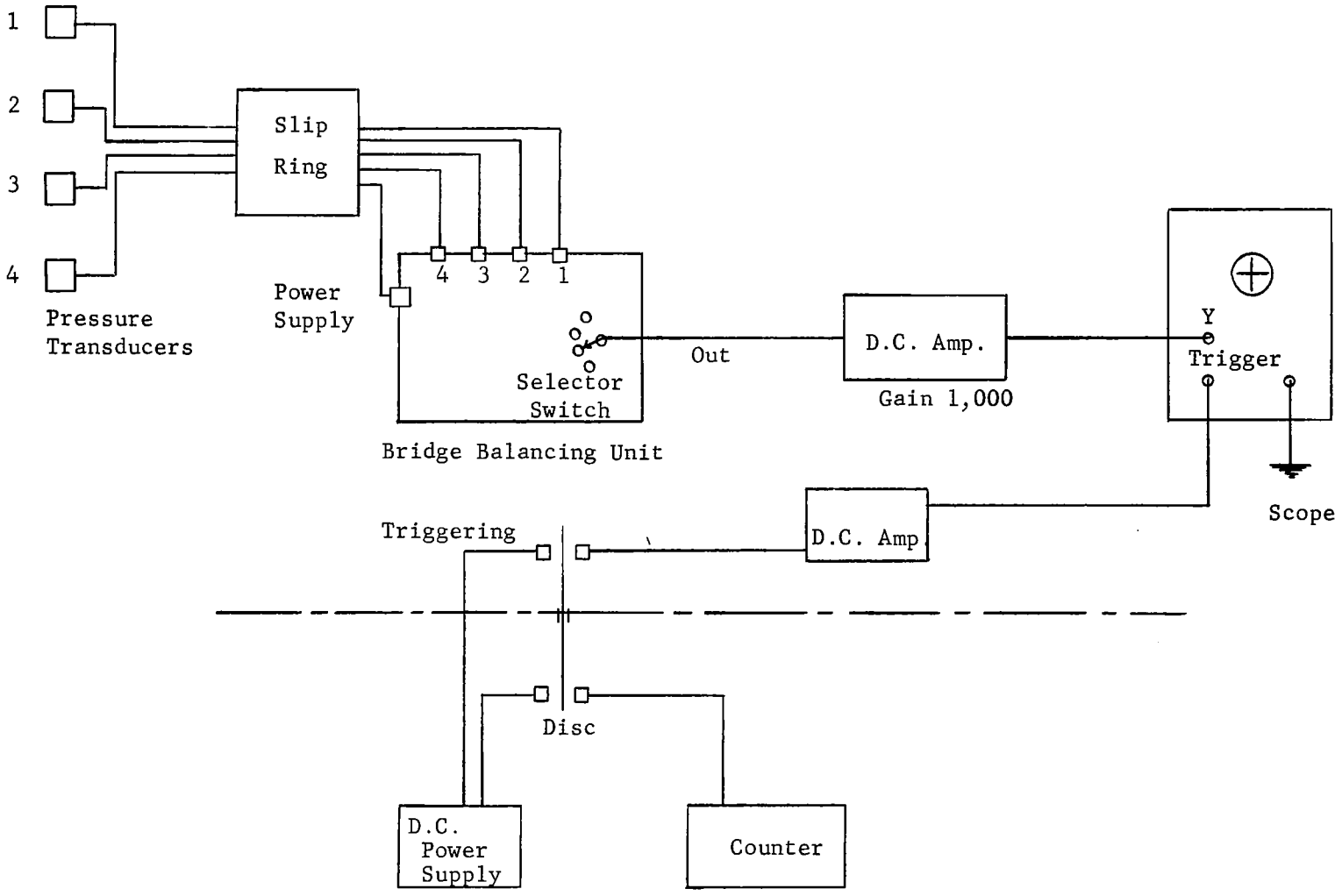

Fig. 9 Block Diagram of the Wiring

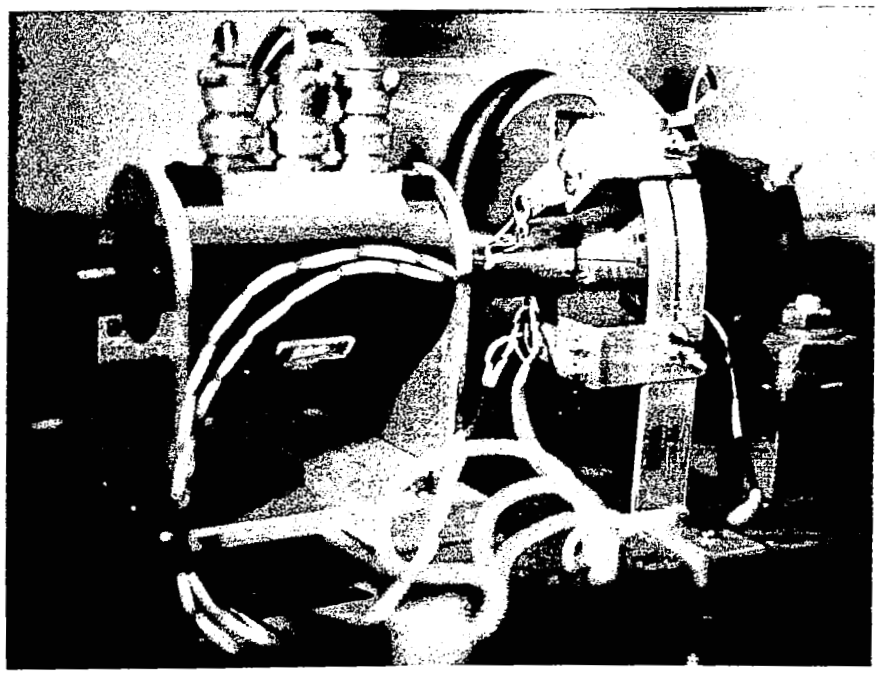

Fig. 10 Counting and Triggering Mechanism

Triggering was necessiated because the time involved in passing through the vortex system was approximately 3 milliseconds. In order to analyse the results occurring during this period, the signal must be triggered just before intersecting the vortex so that the signal can be expanded on the time scale. This was achieved by using another light source and photo cell system similar to the previous one mounted on the same slotted arch.

An 1/8" diameter hole on the same disc at a different radius was used for triggering the scope. Whenever this hole passed in line with the second photo cell system, a pulse was produced. This pulse was fed to the external trigger of the scope and, by adjusting the trigger level and free run mode, the horizontal sweep was triggered.

The second photo cell system was adjustable on the slotted semi-circular arch such that it triggered the scope for all positions of shaft and spanwise location of the gauges before vortex intersection.

IV. EXPERIMENTAL INVESTIGATION

The experimental program was conducted in the 2-1/2 ft by 3 ft subsonic wind-tunnel of the Department of Aerospace Engineering at The Pennsylvania State University. A test velocity of 75 miles per hour was used.

The test set-up and the vortex generating wing in the wind-tunnel are shown in Fig. 11. Four pressure sensors were cemented flush in milled recesses at a radial station of 0.95 and chordwise percentage locations of 6.25, 28.75, 48.75, and 68.75 (Fig. 4b and 4c) and potted with 3M caulking compound No. EC 1126, finished to the blade profile shape.

With the vortex generator and test set-up in the test section, the tunnel was brought up to the test velocity. The vortex leaving from the generator was observed and approximately located in space by using a tuft at the end of a long rod. Next the shaft was moved such that the vortex axis and the shaft axis lay on a horizontal plane, together forming the reference station for vertical movement of the shaft.

The vortex core axis in the horizontal direction was located by moving the rotor horizontally and at the same time observing the scope screen for the maximum difference. The output from the first pressure sensor was found to be significant even for small interferences.

After a considerable warming up period, the outputs of the sensors were individually zero balanced as described earlier. The triggering photo cell was positioned on the circular arch such that

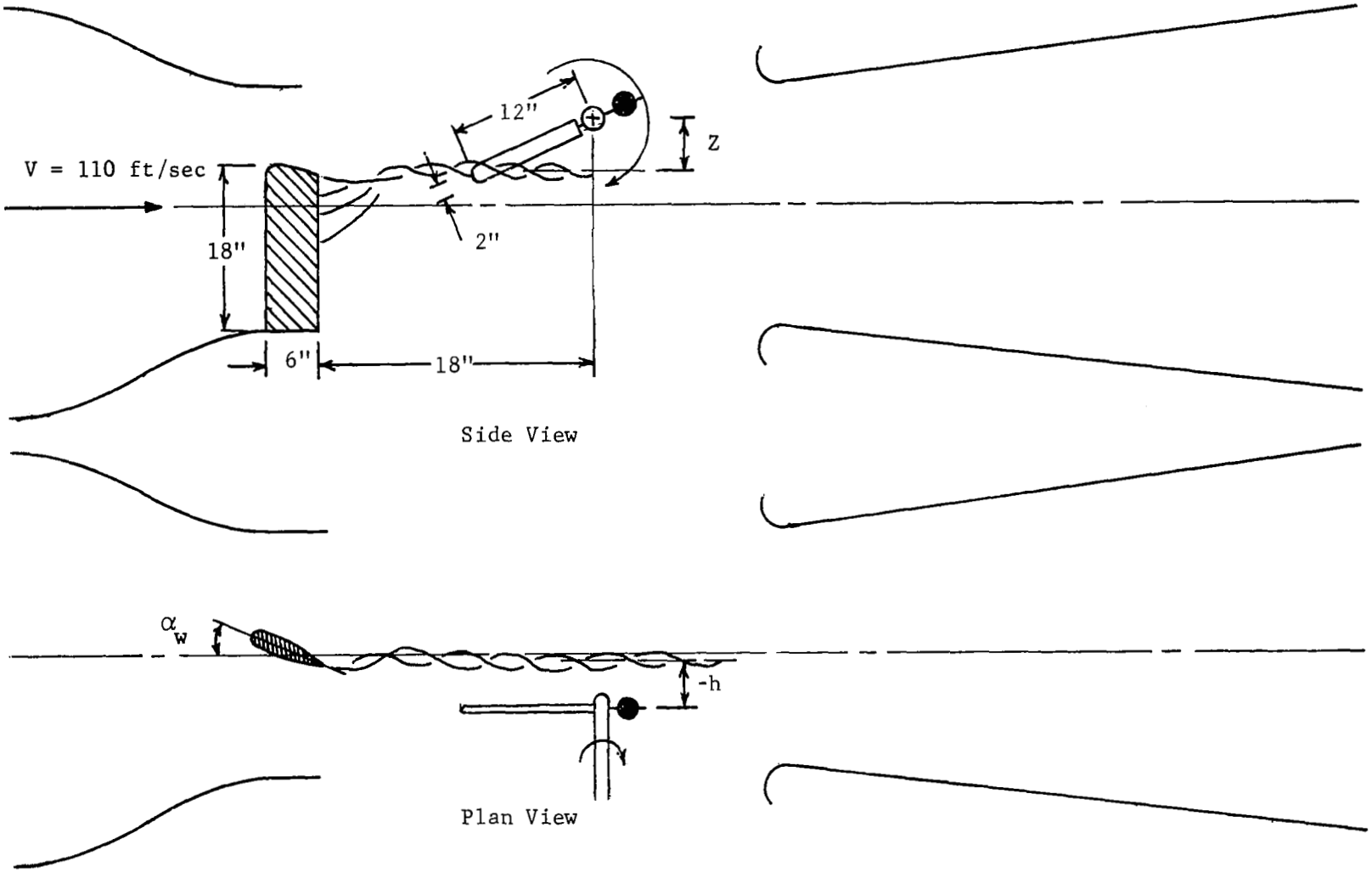

Fig. 11 Schematic Layout of the Test Set-Up in the Wind-Tunnel

the sweep started before the blade came into the vortex field.

Experiments were conducted for four vertical locations of the shaft axis (i.e.) $\frac{Z}{R}$ = 0, 0.25, 0.50 and 0.75, five to six locations of the rotor plane (i.e.) $\frac{h}{c}$ = -1.0 to 1.0, two vortex strengths and structures and two rotational speeds. Results reported in this thesis are for a spanwise station of 0.95R. Additional measurements at the other spanwise locations will be made in the future. The results were recorded on nearly 200 polaroid photographs. Each photograph contained the time wise variation of the pressures of all the four chordwise pressure sensors.

Data Reduction

These traces from the polaroid photographs were read using a trace reader at every 0.2 millisecond intervals with the results being recorded on IBM cards. The results were matched with the corresponding results of the pressures on the other surface of the blade. The matched punched cards were then processed through an IBM 360/67 computer. The results were tabulated in the form of distance travelled in chord lengths, loading/in, section lift coefficient and differential pressure coefficient along the chord at each interval of time.

V. RESULTS AND DISCUSSION

A typical variation of pressures as the blade passes through the vortex at different radial planes is shown in Fig. 12. The intensity of the vortex interaction is seen to decrease as the rotor plane moves away from the center of the vortex. This is as expected since the induced velocity decreases.

Figure 13 shows the variation of the section lift coefficient as the blade cuts through the vortex center. The general shape and trend agree well with that reported in reference (4). The section lift coefficient difference, ΔC_{ℓ}, during a time interval of 1 millisecond was noticed to be as high as 0.7. This time interval corresponds to 1.15 chord lengths travel of the blade. The building up of the load occurs faster than the decay of the load. Generally the blade must be 8 to 10 chord lengths from the vortex before the influence is negligible. This will, of course, depend on the vortex dimensions and the orientation of the blade.

Typical instantaneous chordwise distributions of the differential pressure coefficient are shown in Fig. 14. These are shown at the instant when the blade experiences maximum and minimum peak loads. Results are presented for two vortex strengths. The magnitudes are less for the weaker vortex clearly showing the effect of the induced velocity.

As the blade passes through the vortex, the pressure changes from positive to negative in a typical time interval of 1 millisecond.

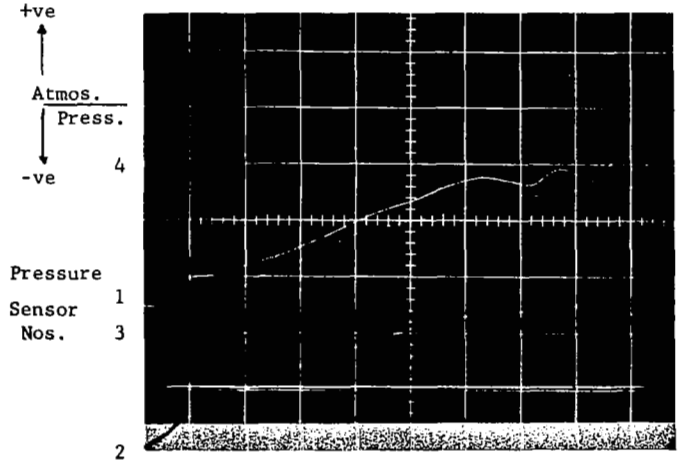

Out of Vortex

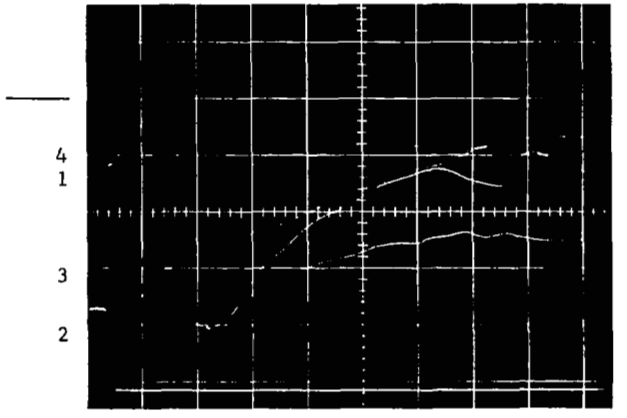

Blade at Center of Vortex

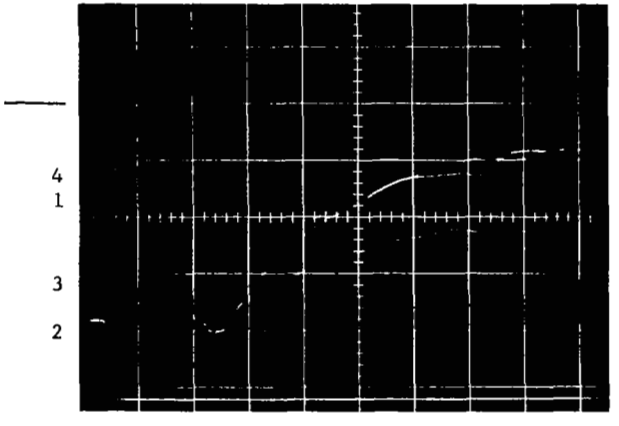

Blade at $\frac{h}{c}$ = 0.25

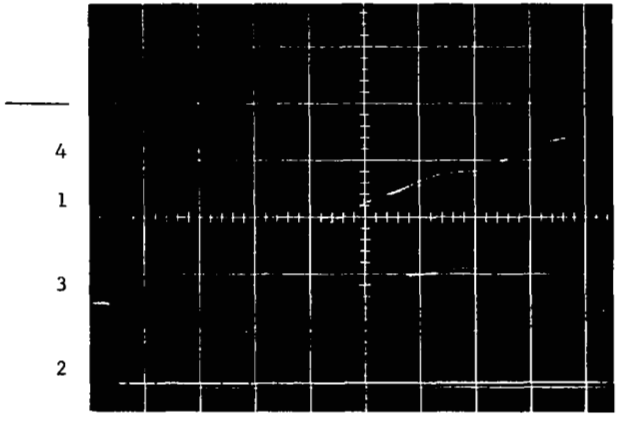

Blade at $\frac{h}{c}$ = 0.5

SCALE

Horizontal 1cm = 1mSec

Vertical:

1. 1cm = .041 psi
2. 1cm = .0467 psi
3. 1cm = .0503 psi
4. 1cm = .0542 psi

Fig. 12 Typical Pressure Traces; RPM = 2000; $\frac{r}{R}$ = 0.95

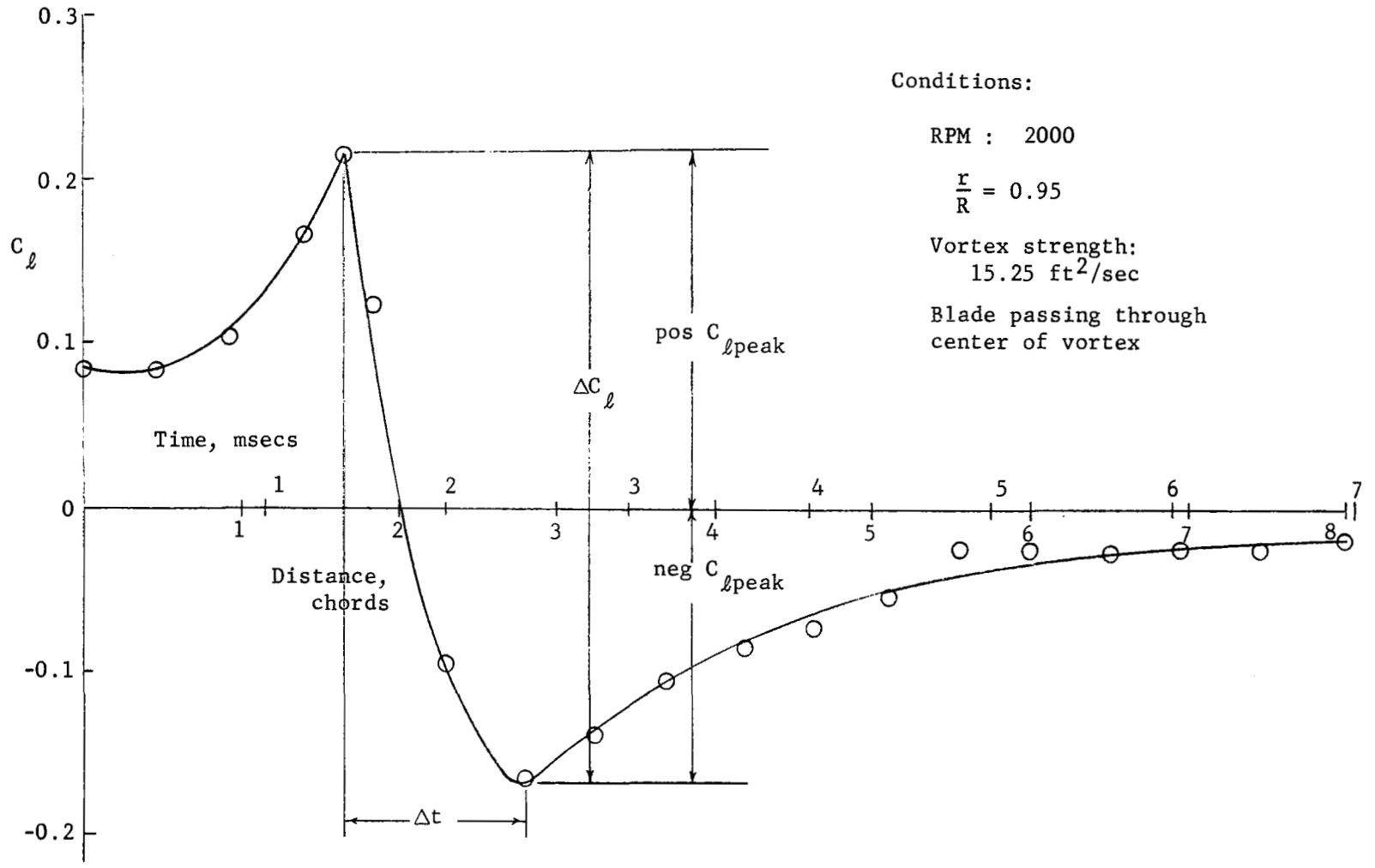

Fig. 13 Typical Section Lift Coefficient Variation on Rotor Blade

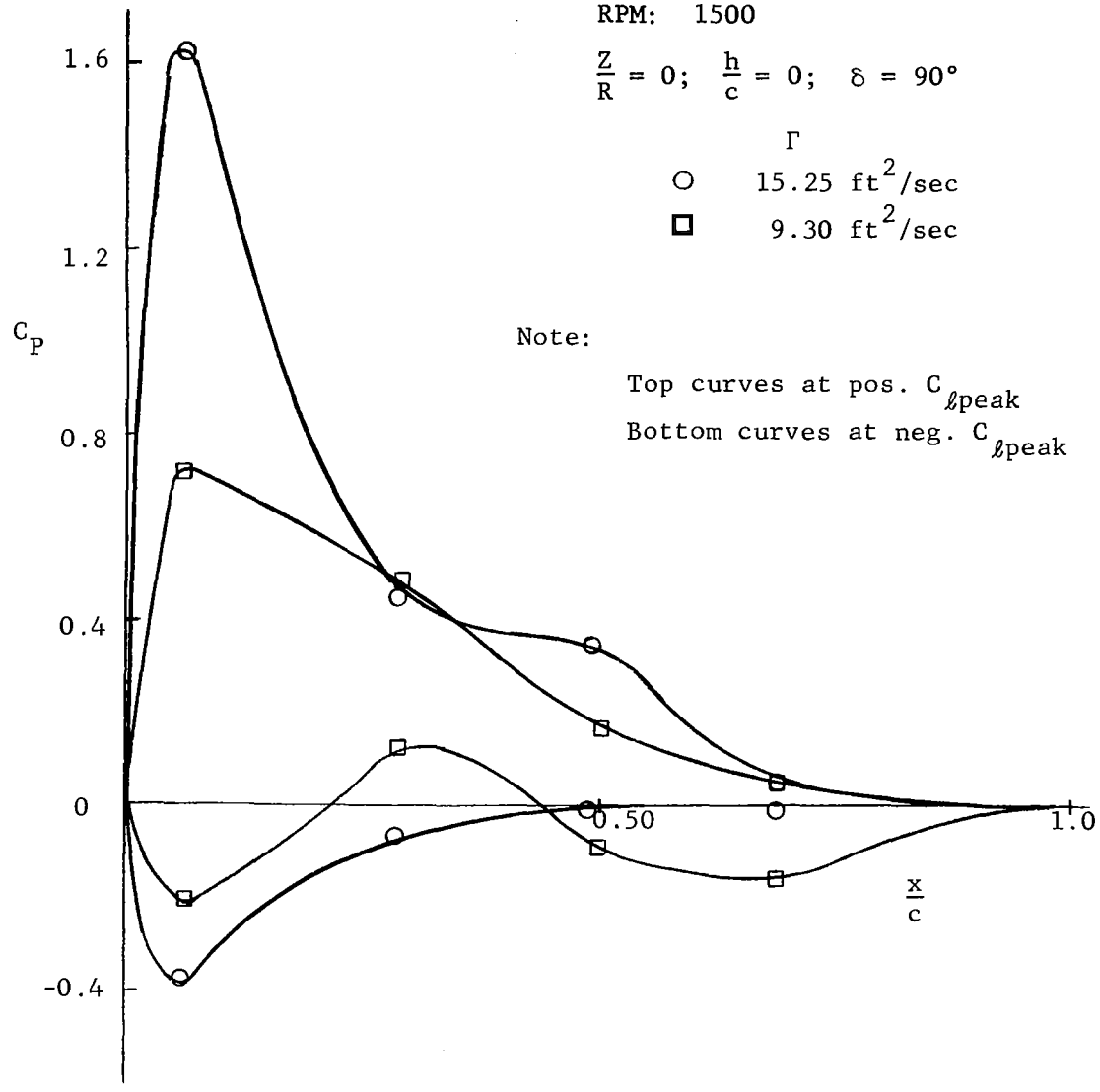

Fig. 14 Chordwise Differential Pressure Coefficient Variation

The pressure distributions are quite irregular, especially for negative lift.

The maximum lift difference and its time variation in a sweep are important for the estimation of the structural and fatigue life of the blade and for the blade slap, i.e., 'bang power' and 'bang energy'. So, for the remaining of the figures the variations of the above two quantities which are defined in Fig. 13 are discussed.

For the two RPM's, the effect of passing through the vortex at various distances from its center is shown in Fig. 15a. The maximum section lift coefficient, ΔC_{ℓ}, decreases as the rotor blade moves away from the vortex axis, unsymmetrically. The values of ΔC_{ℓ} are lower for the lower vortex strength. The asymmetry is due to the unequal resultant velocity and angle of attack which the blade experiences on either side of the vortex. Though the values of ΔC_{ℓ} for the 2000 RPM case are smaller than those for the case of 1500 RPM under similar conditions, the actual lift increments will be greater due to the higher velocity. In Fig. 15b the variation of the maximum angle of attack difference in a sweep with radial distance is shown for the two RPM values tested. Like the lift variation, these angles also vary unsymmetrically on either side of the vortex center.

Figure 16 shows the variation of ΔC_{ℓ} with rotor plane position, $\frac{h}{c}$, for various positions of shaft axis, $\frac{Z}{R}$, for each of the two RPM's tested. As explained earlier, the values for the higher RPM are lower compared to the lower RPM. When compared at a particular RPM, the maximum section lift coefficient difference, ΔC_{ℓ}, increases slightly as the axis of rotation, $\frac{Z}{R}$, is moved from vortex center.

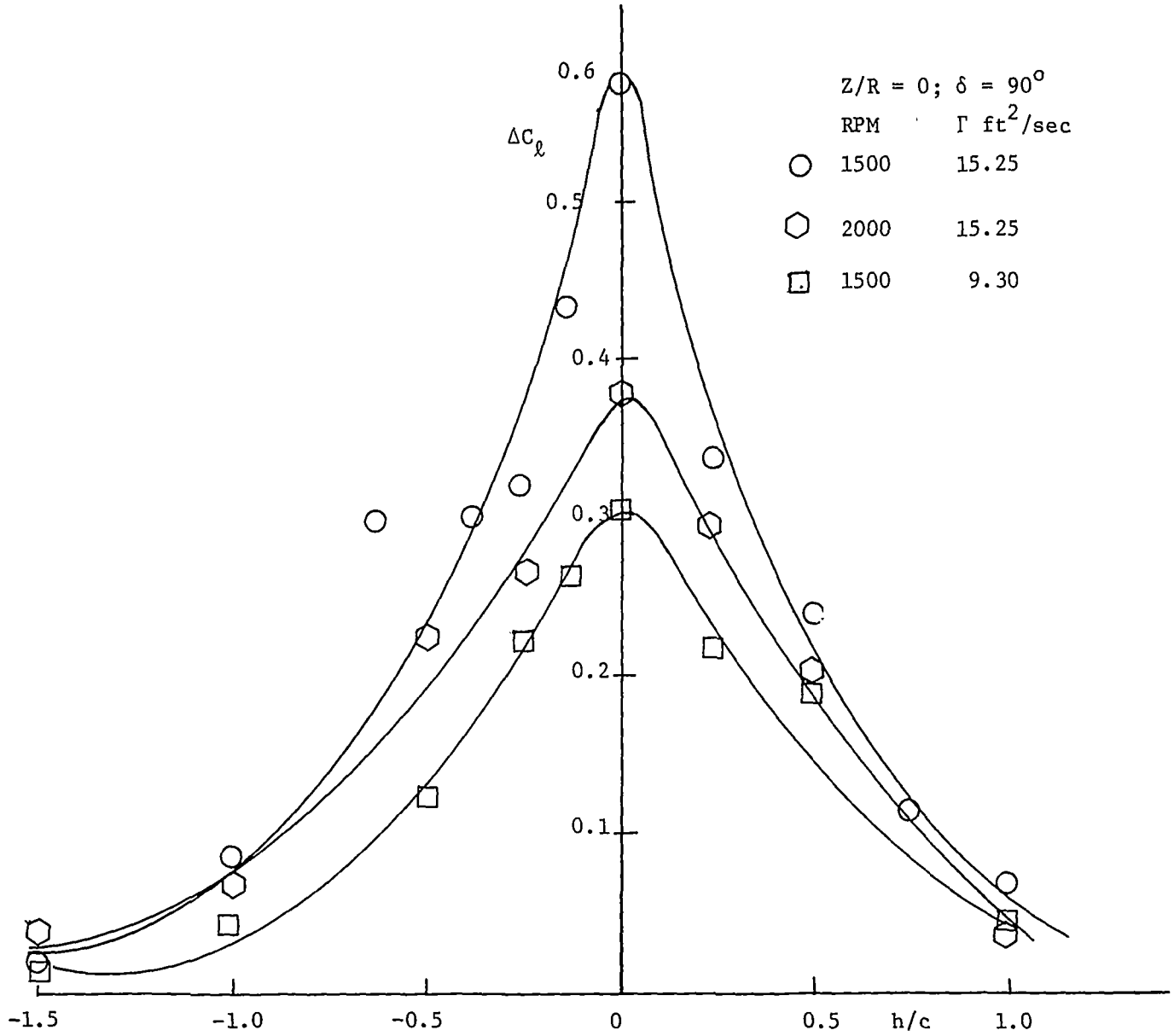

Fig. 15a Variation of Maximum Section Lift Coefficient Difference with Rotor Plane Position

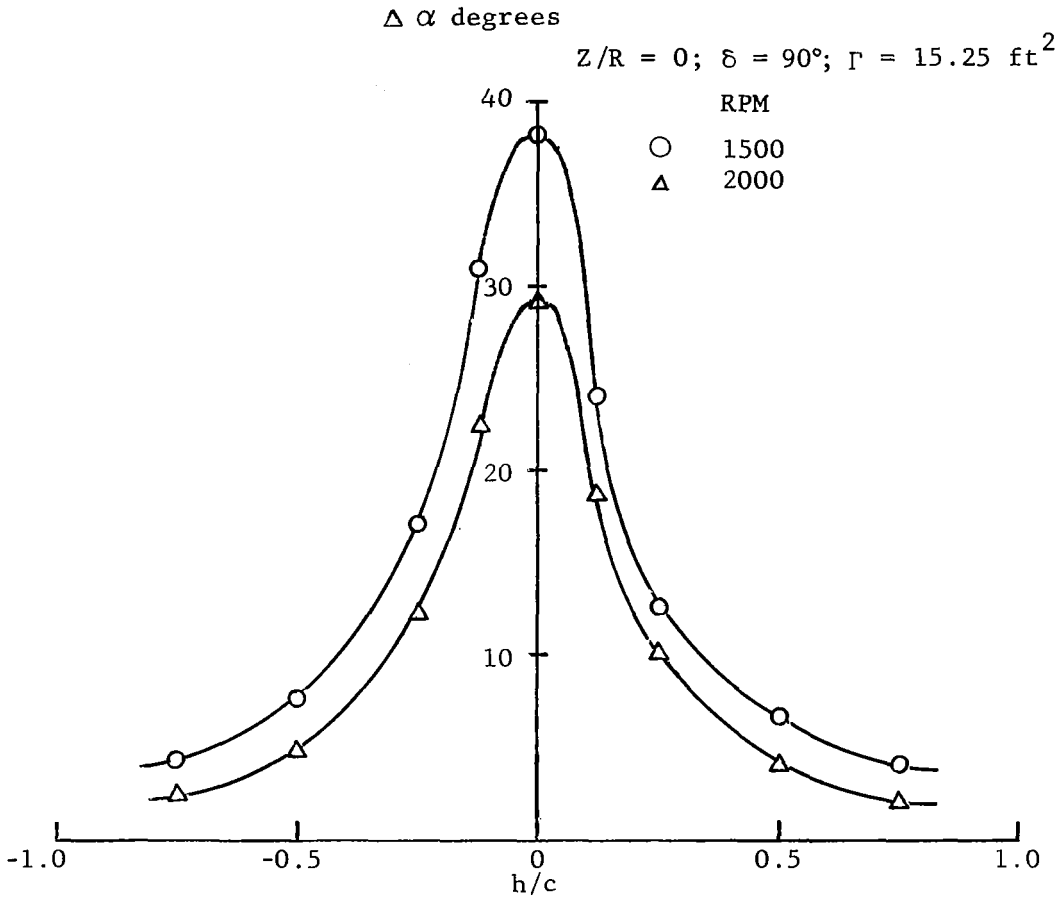

Fig. 15b Variation of Maximum Angle of Attack Change with Radial Distance

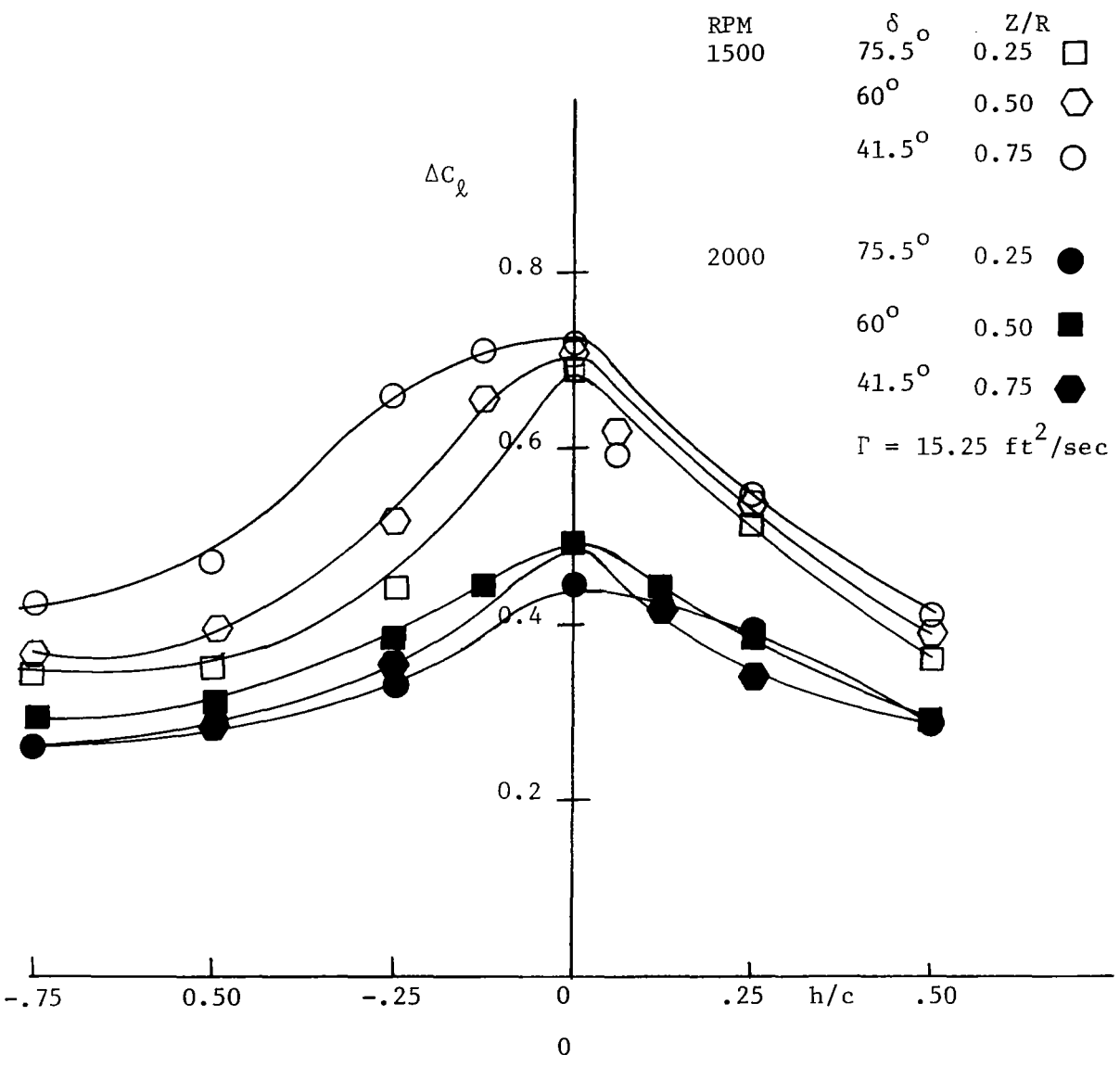

Fig. 16 ΔC_ℓ vs h/c for Constant Intersection Angles

These increments in ΔC_ℓ are due to two factors: one is the increased velocity, i.e., addition of VSin ψ to ωr, while the other is the increased size of the vortex as the blade passes. Using equations A.1 and A.2 of Appendix, it is noticed that the difference, ΔL, increases with increasing vortex size. These increments are smaller for the positive radius side of the vortex than those for the negative side. These positive and negative radius directions are defined in Fig. 1 with respect to the rotational direction of vortex.

A sample of peak positive and negative lift coefficient variations (see Figs. 1 and 13) as the blade cuts through the vortex at various radial distances from the vortex center are shown in Fig. 17 for two positions of the shaft axis, $\frac{Z}{R}$. The individual peak values occur approximately when h is zero but the curves are unsymmetrical. The negative peak lift coefficient increases and the positive lift coefficient decreases as the intersection angle, δ, decreases. It is also noticed from the above figure that the negative peak section lift coefficient for the case of $\delta = 41.5°$ is as great in magnitude as the positive peak lift coefficient for $\delta = 90°$.

It is shown in reference 15 that the total sound energy per unit time radiated into the far field is proportional to the square of the time-rate-change of the fluctuating load per unit span. The 'bang power' and 'bang energy' also depend on these time rate changes.

The variation of this time-rate-change, $\frac{\Delta C_\ell}{\Delta t}$, with rotor plane position, $\frac{h}{c}$, for the two values of RPM's and the vortex strengths, are shown in Figs. 18a and 18b. The general variation and trend is similar to that of the ΔC_ℓ (Fig. 15a). There is a considerable decrease

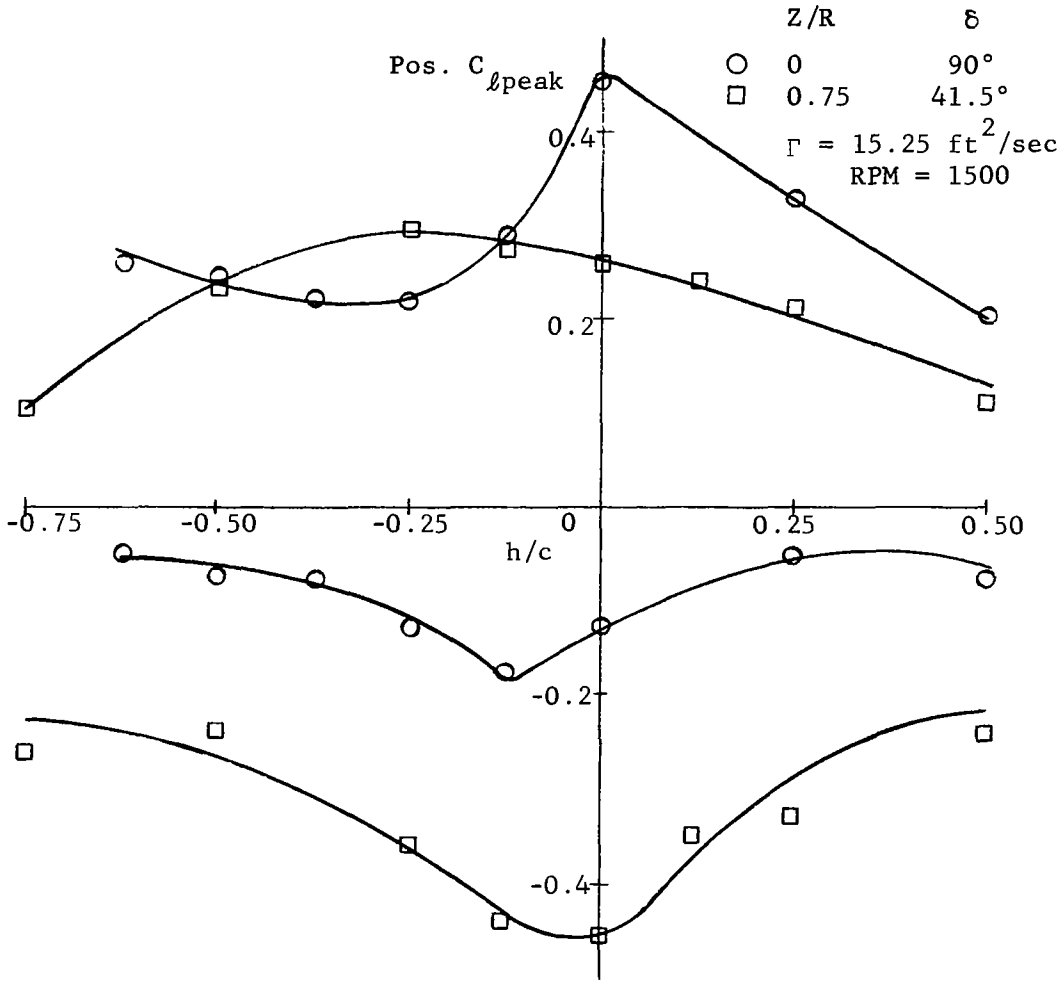

Fig. 17 Peak Section Lift Coefficient vs Rotor Plane Position

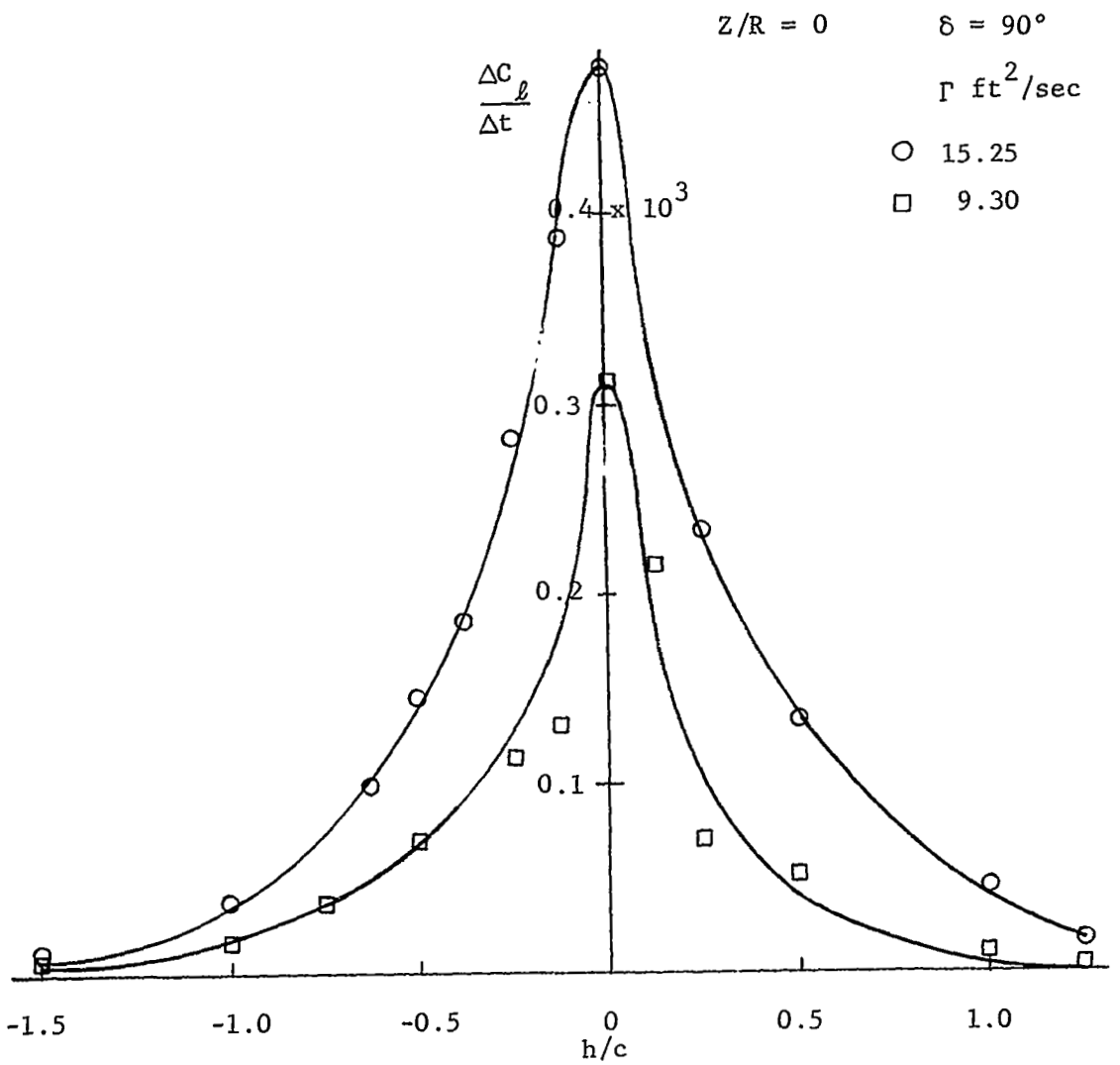

Fig. 18a Time-Rate-Changes of ΔC_ℓ with Rotor Plane Position; RPM = 1500

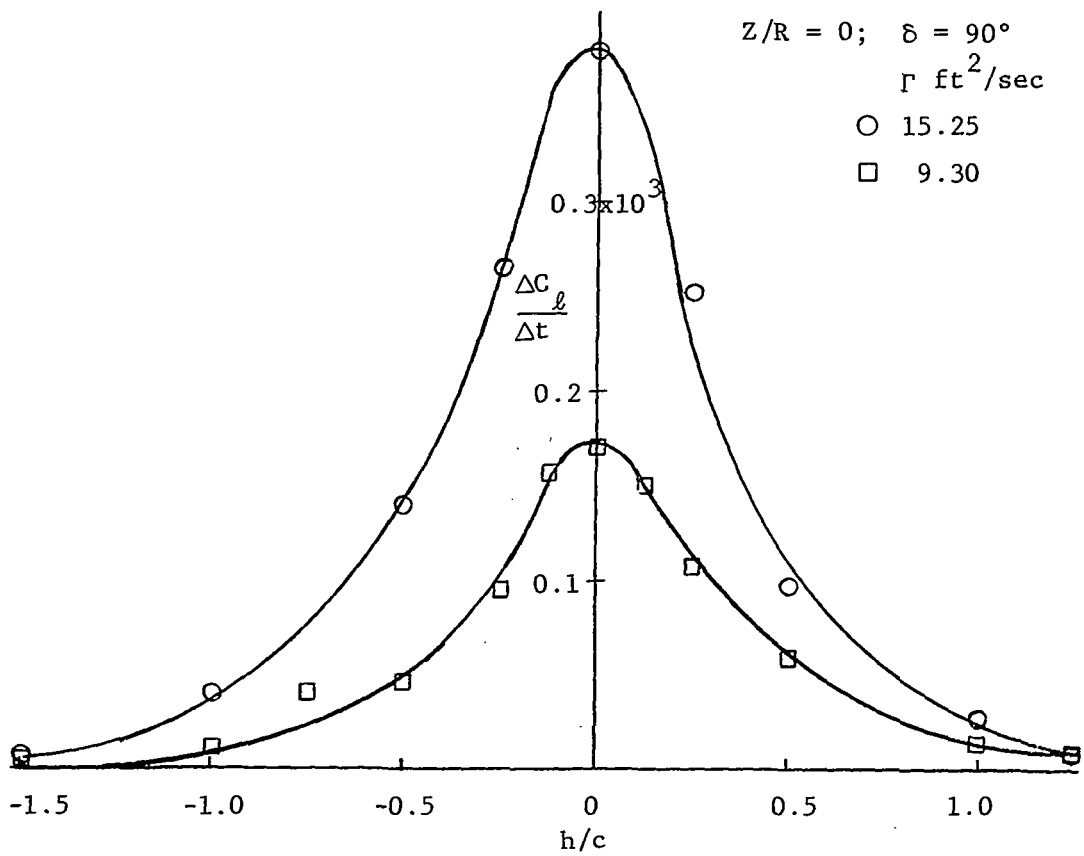

Fig. 18b Time-Rate-Changes of ΔC_ℓ with Rotor Plane Position; RPM = 2000

in the rate, $\Delta C_\ell/\Delta t$, with decrease in vortex strength. It has been observed experimentally[16] that the maximum induced velocity in a vortex increases linearly with increasing angle of attack, whereas the width shows little change for a standard tip wing. When comparing the results $(\frac{\Delta C_\ell}{\Delta t})$ at a constant RPM for two vortex generating wing angles, the vortex induced velocity changes considerably whereas the impulsive time changes very little. Therefore the time-rate-change varies considerably when the two vortex strengths are compared. The variations of the time-rate-changes of section lift coefficients, $\frac{\Delta C_\ell}{\Delta t}$, for different positions of the rotor axis, $\frac{Z}{R}$, at the two RPM's tested are shown in Figs. 19a and 19b. The curves drop off on either side of the center of the vortex and all the peak values occur near the center, as expected.

The variations of these two parameters, ΔC_ℓ and $\frac{\Delta C_\ell}{\Delta t}$ with rotor axis positions, $\frac{Z}{R}$, are shown more explicitly for the two values of RPM tested in Figs. 20a and 20b. This rotor axis position, $\frac{Z}{R}$, in turn fixes the intersection angle as defined earlier. For example, $\frac{Z}{R} = 0$ gives an intersection angle of 90 degrees, i.e., the blade is completely in the vortex field and, for $\frac{Z}{R} = 1$, the intersection angle is zero degrees. The maximum section lift coefficient difference, ΔC_ℓ, increases with decreasing intersection angle. The same result has been reported in reference (13). However, the time-rate-changes reach their maximum values at a $\frac{Z}{R}$ value of 0.25 which corresponds to a δ of 75.5° and thereafter drops off gradually. These trends are also evident for the other RPM value and for various vortex radii positions. Similar trends are also obtained using equations (A.1) and (A.2) of the

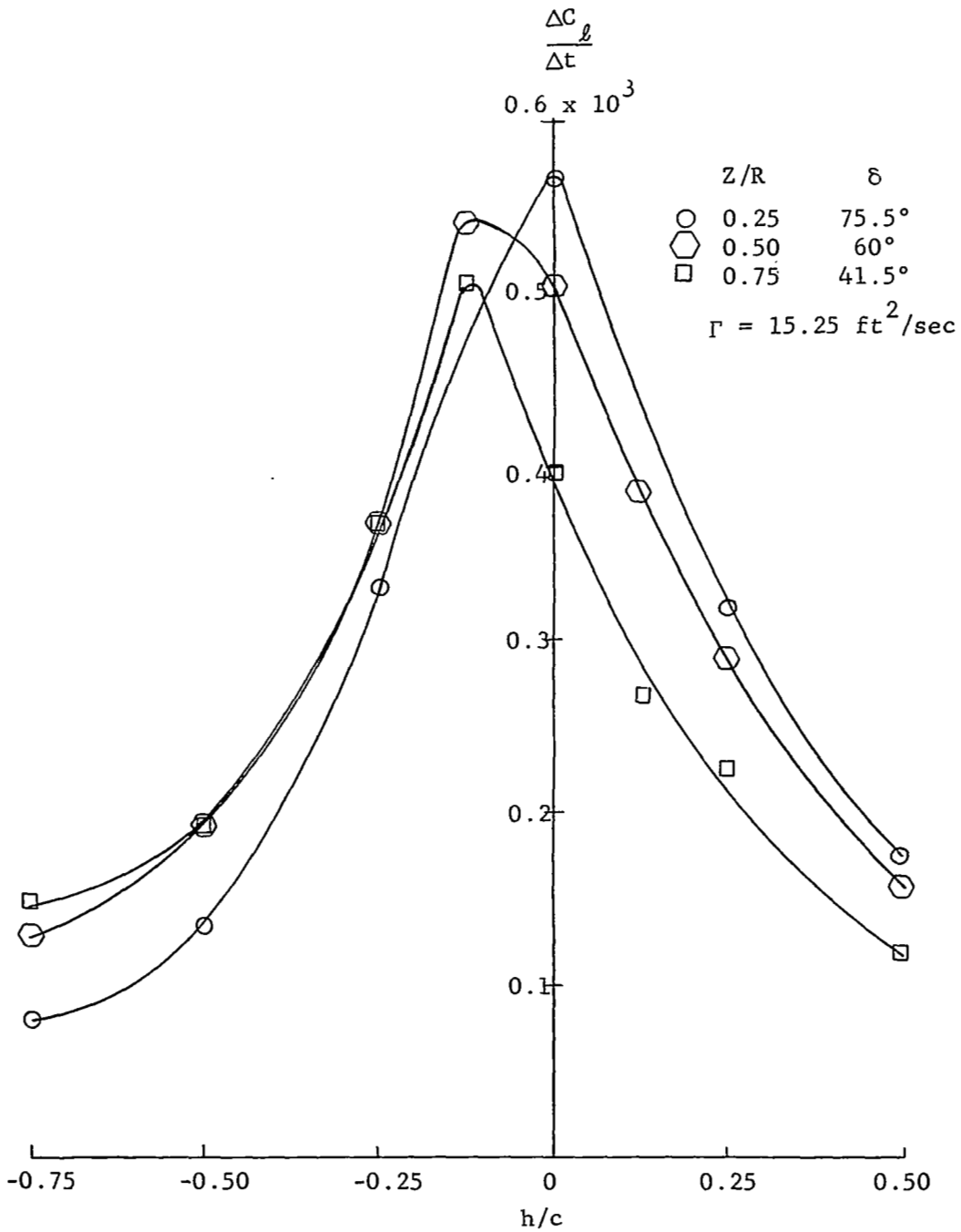

Fig. 19a $\frac{\Delta C_\ell}{\Delta t}$ vs Rotor Plane Position; RPM = 1500

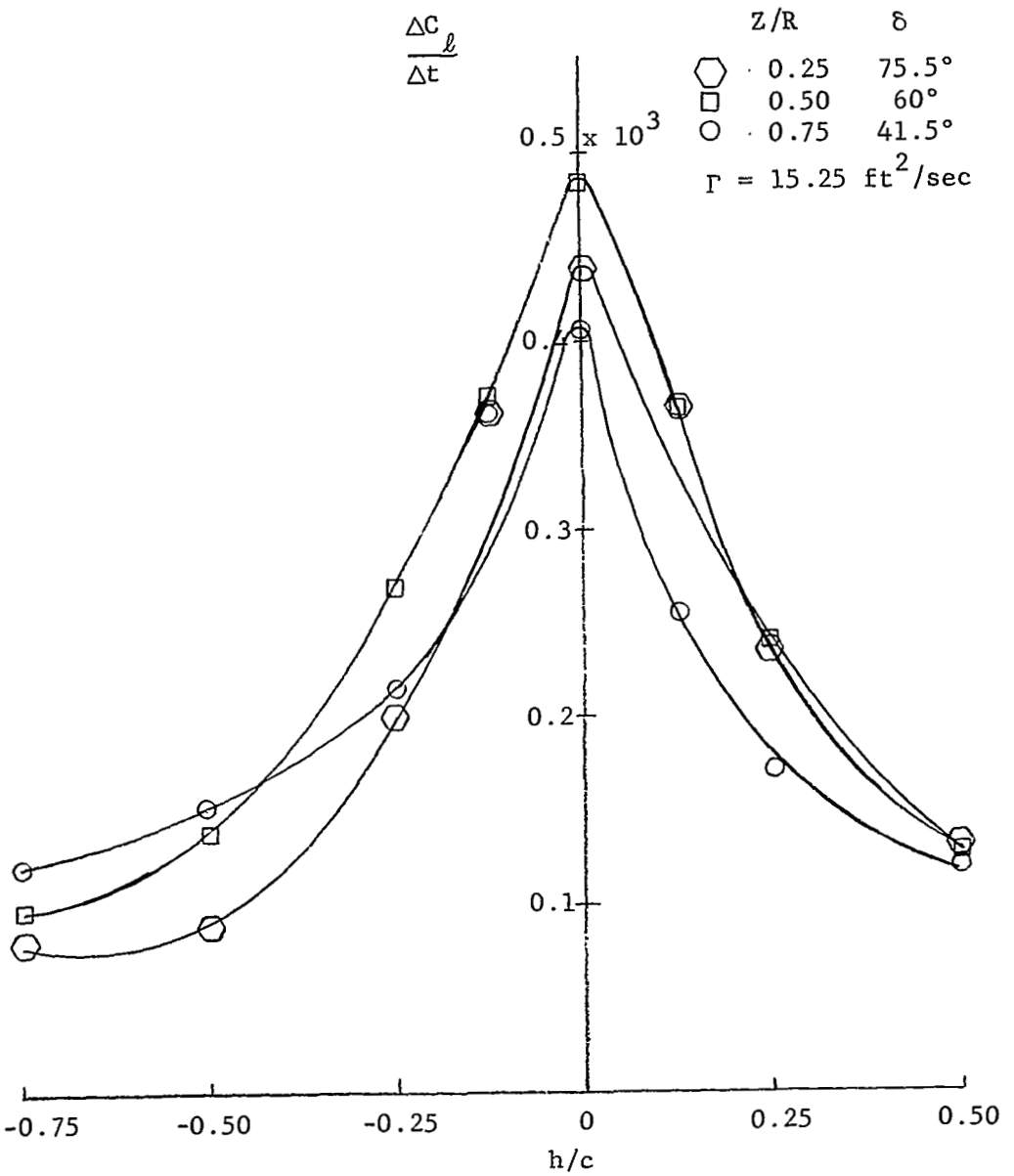

Fig. 19b $\frac{\Delta C_\ell}{\Delta t}$ vs Rotor Plane Position; RPM = 2000

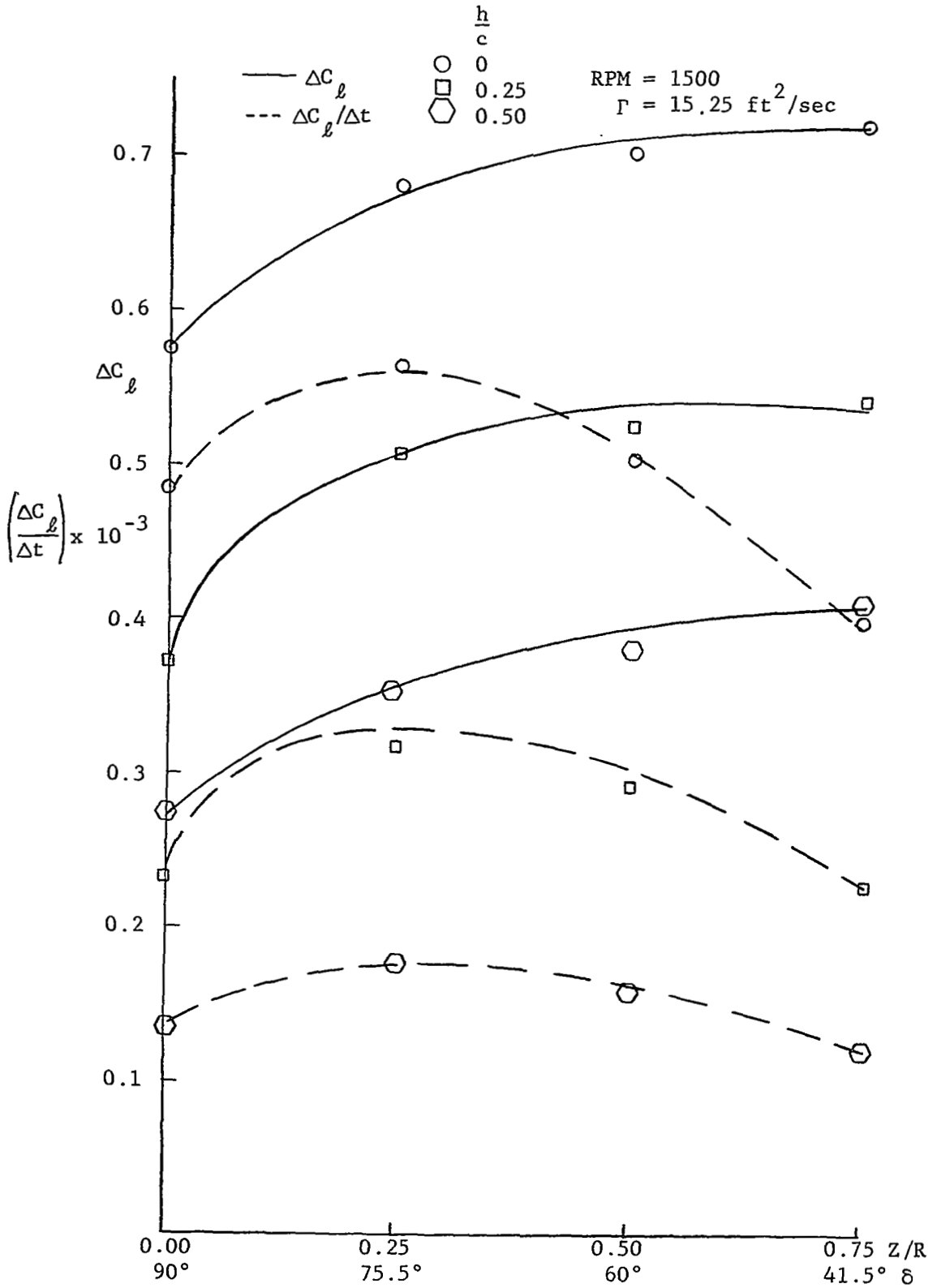

Fig. 20a Variation of ΔC_ℓ and $\frac{\Delta C_\ell}{\Delta t}$ with Intersection Angle

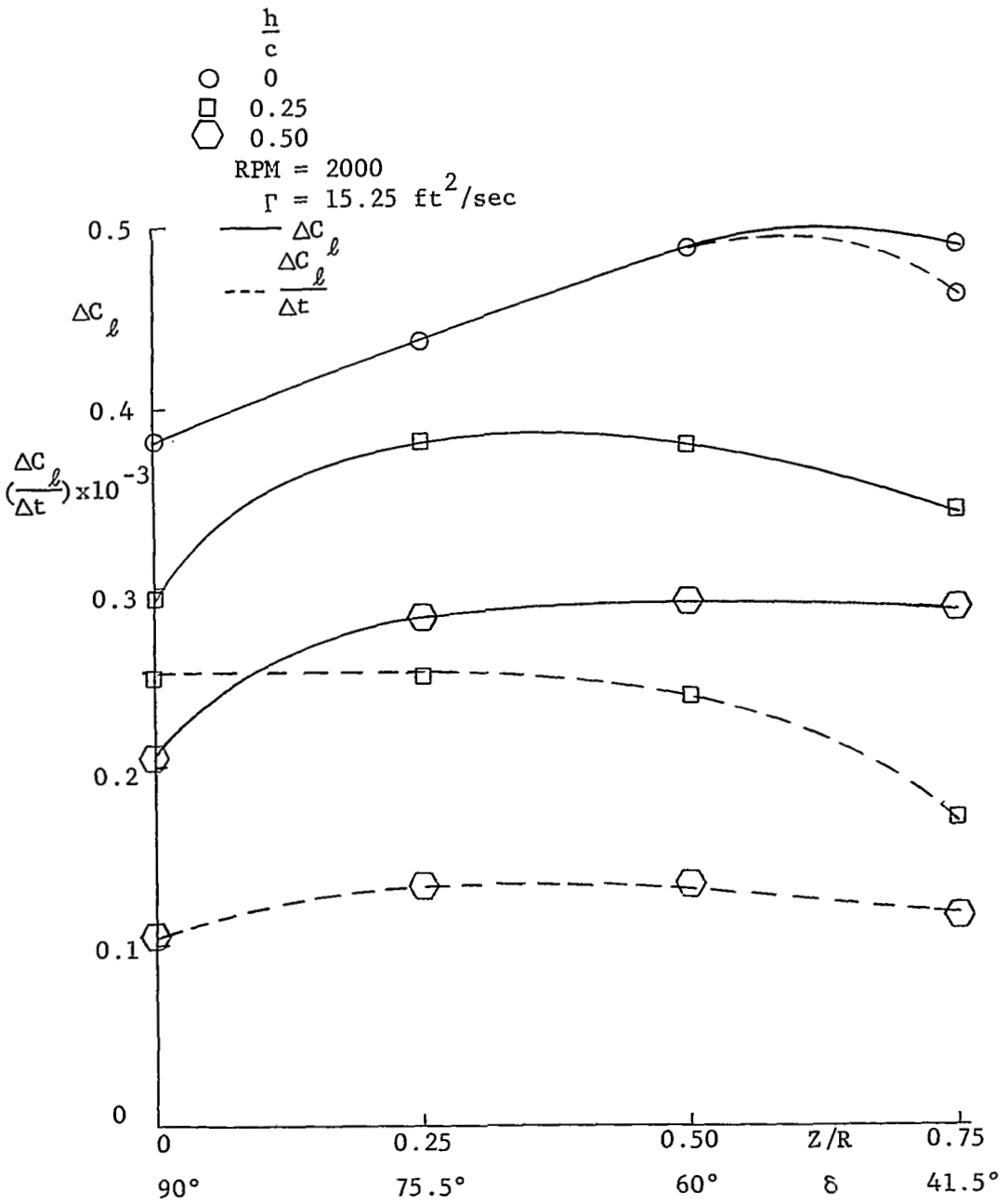

Fig. 20b Variation of ΔC_ℓ and $\frac{\Delta C_\ell}{\Delta t}$ with Intersection Angle

appendix when applied to the vortex-induced velocity profiles which the blade experiences for different intersection angles.

The effect of vortex strength on these two parameters, namely ΔC_ℓ and $\frac{\Delta C_\ell}{\Delta t}$, is shown in Figs. 21a and 21b for the case of Z/R = 0 and for different rotor plane positions $(\frac{h}{c})$. The vortex strengths are non-dimensionalized with tip velocity and the radius of the blade. It is noticed that both parameters increase linearly, giving different slopes for different h/c locations. The maximum slope of these two parameters occurs when the blade passes through the center of the vortex, thus indicating maximum changes.

Simplified Quasi-Steady Analysis

A simplified analysis can be made from geometrical considerations for the blade passing through a vortex with its full span in the vortex. Consider Fig. 22 which shows schematically the various velocity components acting on the blade. For the general case, when the blade is passing through the vortex at a radial distance h from the center, the blade experiences an angle of attack α given by

$$\tan \alpha = \frac{v_\theta(r) \left(1 - \frac{h^2}{r^2}\right)^{1/2}}{V_r \pm v_\theta(r) \frac{h}{r}} \qquad (5.1)$$

where V_r is the velocity of the blade at a spanwise station r. The positive or negative sign corresponds to the blade passing through the positive or negative radius side of the vortex as defined in Fig. 1.

For small angles, $\tan \alpha = \alpha$ in radians

$$C_\ell = a_o \alpha$$

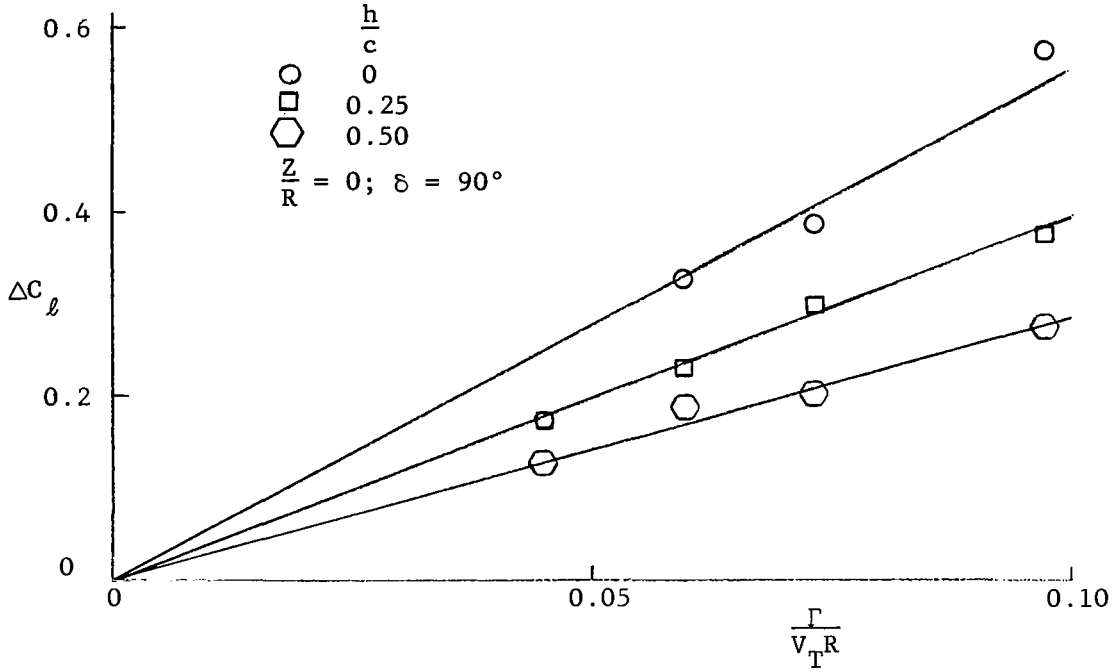

Fig. 21a Variation of ΔC_ℓ with circulation

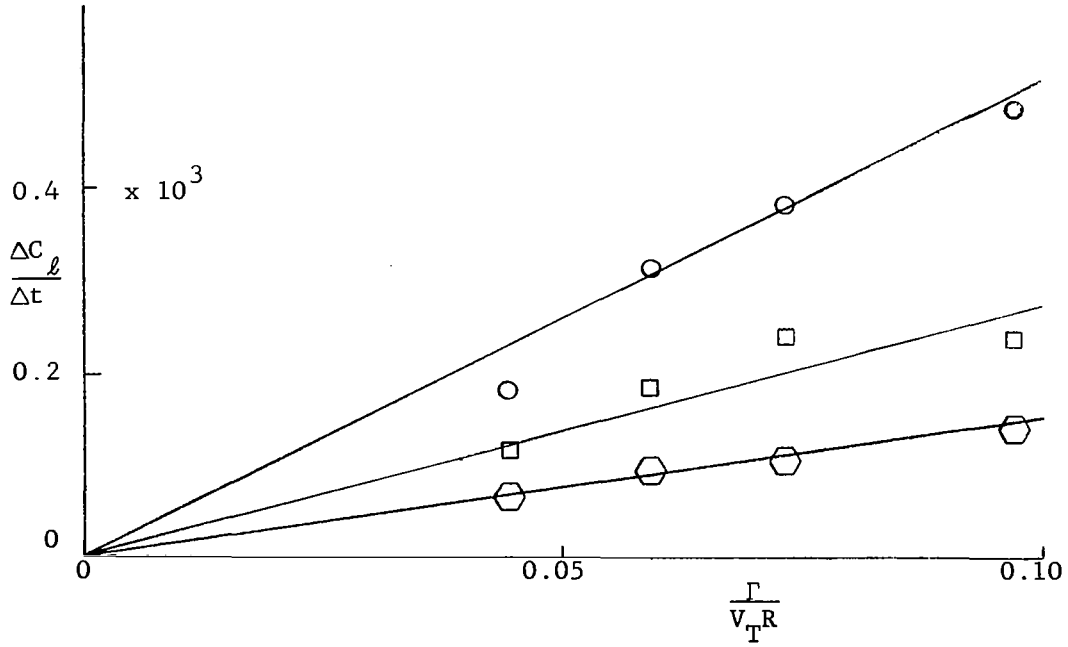

Fig. 21b Variation of $\frac{\Delta C_\ell}{\Delta t}$ with Circulation

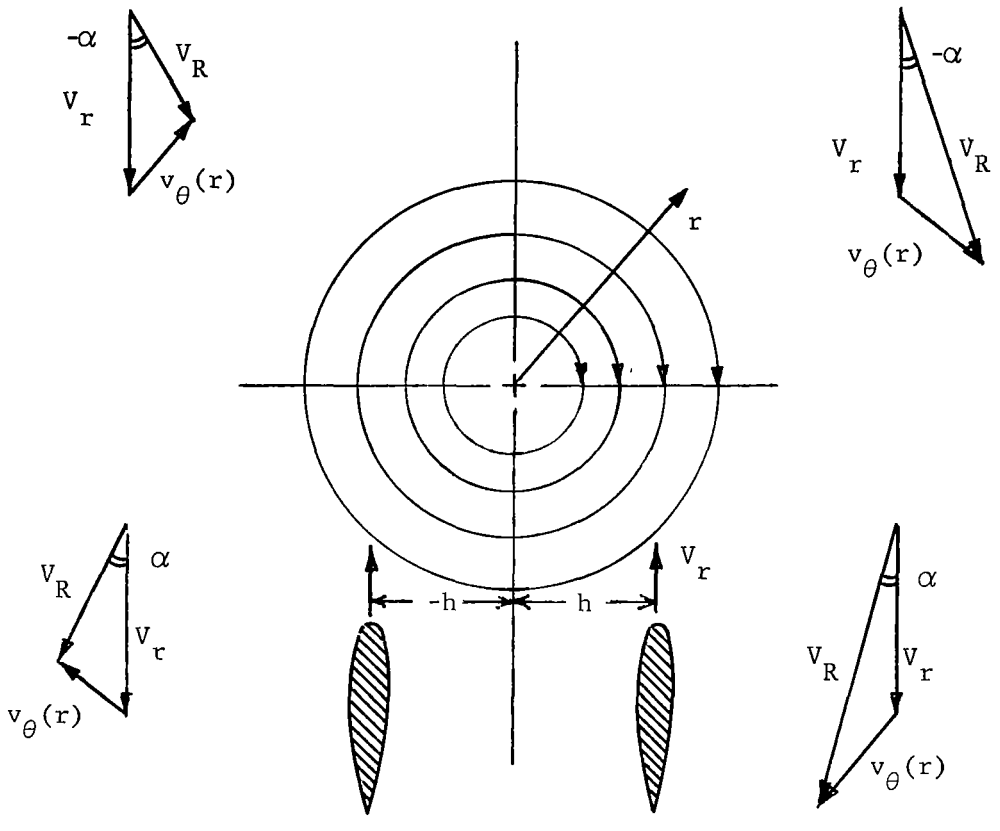

$$\tan\alpha = \frac{v_\theta(r)\ (1-\frac{h^2}{r^2})^{1/2}}{V_r - v_\theta(r)\ \frac{h}{r}} \qquad \tan\alpha = \frac{v_\theta(r)\ (1-\frac{h^2}{r^2})^{1/2}}{V_r + v_\theta(r)\ \frac{h}{r}}$$

Fig. 22 Vector Diagram of Velocity Components

where a_o is lift curve slope, 5.71/radian

$$C_\ell = a_o \frac{v_\theta(r)\ (1 - \frac{h^2}{r^2})^{1/2}}{V_r \pm v_\theta(r)\ \frac{h}{r}} \tag{5.2}$$

According to reference 2,

$$\Gamma = \Gamma(a)\ \ell n(\tfrac{r}{a}) + \Gamma(a) \tag{5.3}$$

except for a small eye at the center of the vortex. In terms of velocity

$$r\ v_\theta(r) = a\ v_\theta(a)\ \ell n(\tfrac{r}{a}) + a\ v_\theta(a)$$

$$\frac{v_\theta(r)}{v_\theta(a)} = \frac{\ell n(\frac{r}{a}) + 1}{(\frac{r}{a})} \tag{5.4}$$

Substituting in the equation (5.2)

$$C_\ell = a_o \frac{v_\theta(a)}{V_r} \left[\frac{\frac{\ell n(\frac{r}{a}) + 1}{(r/a)} \left(1 - \frac{h^2}{r^2}\right)^{1/2}}{1 + \frac{v_\theta(a)}{V_r} \left\{ \frac{\ell n(r/a) + 1}{(r/a)} \right\} \frac{h}{r}} \right] \tag{5.5}$$

For the case of the blade passing through the center of the vortex (i.e.) h = 0

$$C_\ell = a_o \frac{v_\theta(a)}{V_r} \left[\frac{\ell n(\frac{r}{a}) + 1}{(r/a)} \right] \tag{5.6}$$

and the peak value of C_ℓ, when r = a, is

$$C_{\ell peak} = a_o \frac{v_\theta(a)}{V_r} \tag{5.7}$$

Therefore
$$\frac{C_{\ell}}{C_{\ell peak}} = \frac{\frac{\ell n(\frac{r}{a}) + 1}{(r/a)} \left(1 - \frac{h^2}{r^2}\right)^{1/2}}{1 + \frac{v_{\theta}(a)}{V_r}\left[\frac{\ell n(r/a) + 1}{(r/a)}\right]\frac{h}{r}} \qquad (5.8)$$

For comparison with the experimental results, distance travelled in terms of chord lengths is given by $\frac{r}{c} = \frac{(\frac{r}{a})}{(\frac{c}{a})}$ for the blade passing through the center of the vortex and $\frac{x}{c} = \frac{(\frac{r}{a})}{(\frac{c}{a})}(1 - \frac{h^2}{r^2})^{1/2}$ for the rotor plane at a distance of h from the center of the vortex.

It should be noted that the theoretical peak value of the section lift coefficient obtained from the approximate analysis overestimates the experimental peak value. The values are tabulated in Table 1. However equation (5.8) does predict the variation of the ratio of section lift coefficient to peak section lift coefficient as the blade cuts through a vortex. So the above equation (5.8) is evaluated using the individual experimental peak section lift coefficients. These are compared with the experimental results in Figs. 23a,b,c for values of $\frac{h}{c}$ = 0, 0.25, -0.25 respectively where the agreement is seen to be surprisingly good.

Table 1

Theoretical and Experimental Peak
Section Lift Coefficient Values

$\frac{h}{c}$	$C_{\ell peak}$ (Theory)	$+C_{\ell peak}$ (Experiment)	$-C_{\ell peak}$ (Experiment)	Fig.
0	1.493	0.225	0 170	23a
0.25	0.940	0.225	0.075	23b
-0.25	1.140	0.125	0.130	23c

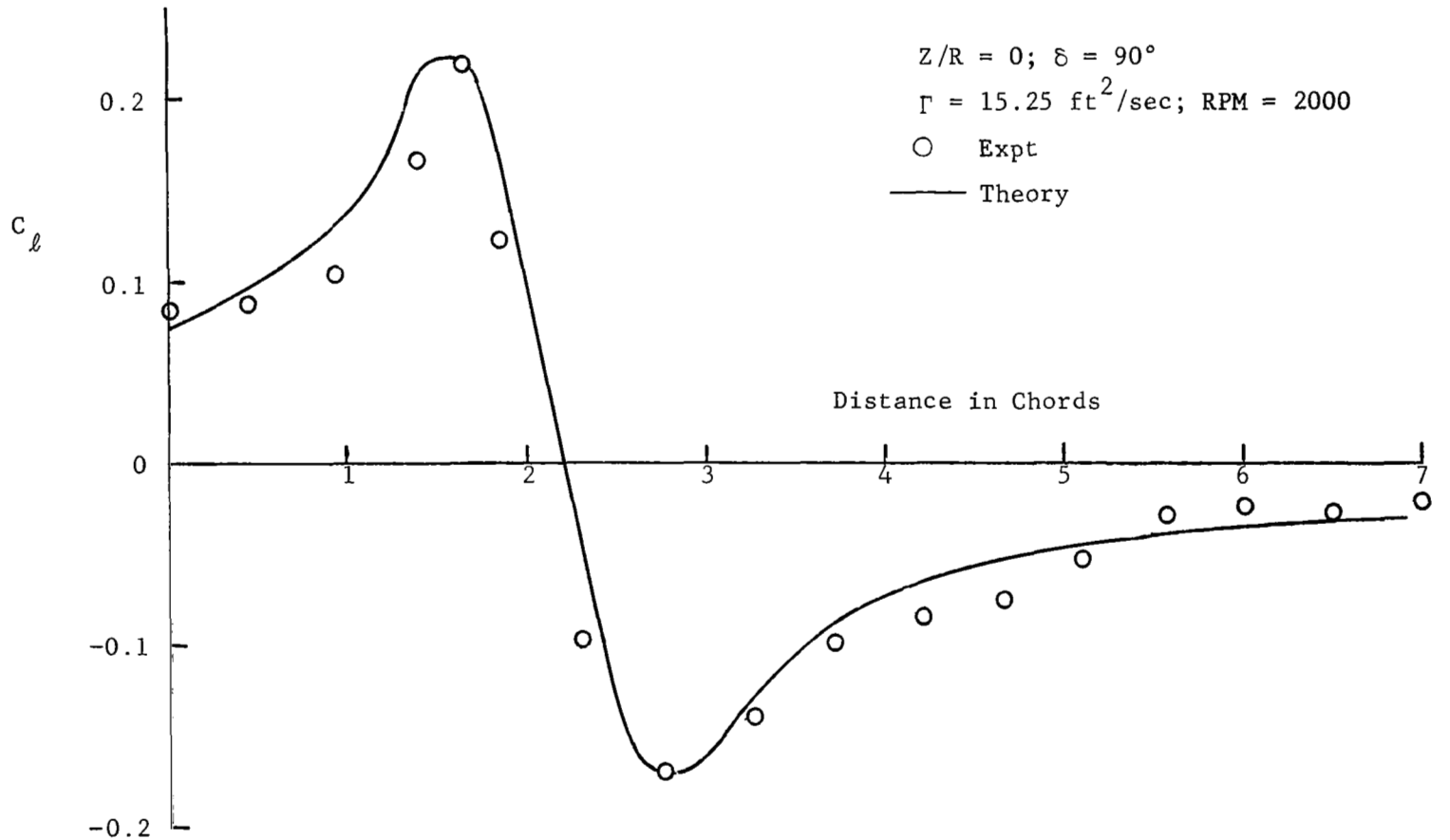

Fig. 23a Section Lift Coefficient Variation Through the Vortex
h/c = 0.0

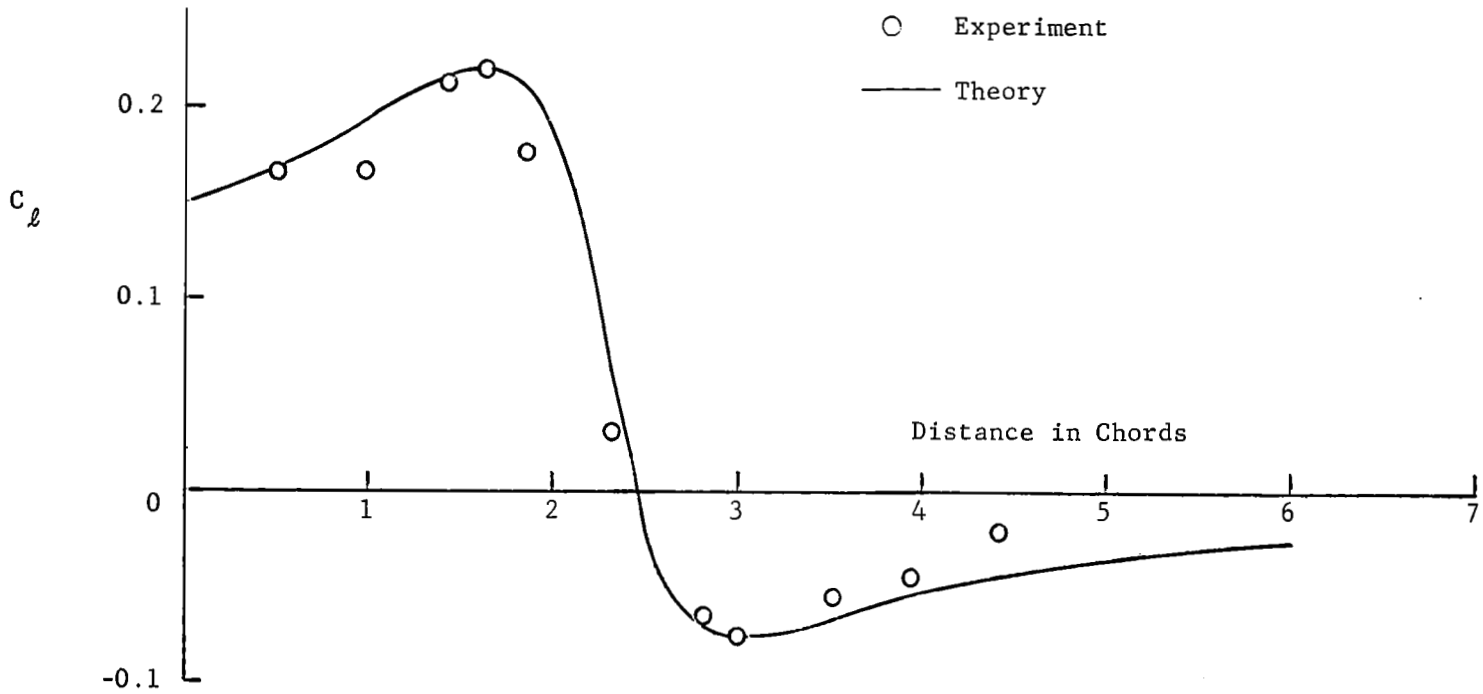

Fig. 23b Section Lift Coefficient Variation Through the Vortex; h/c = 0.25

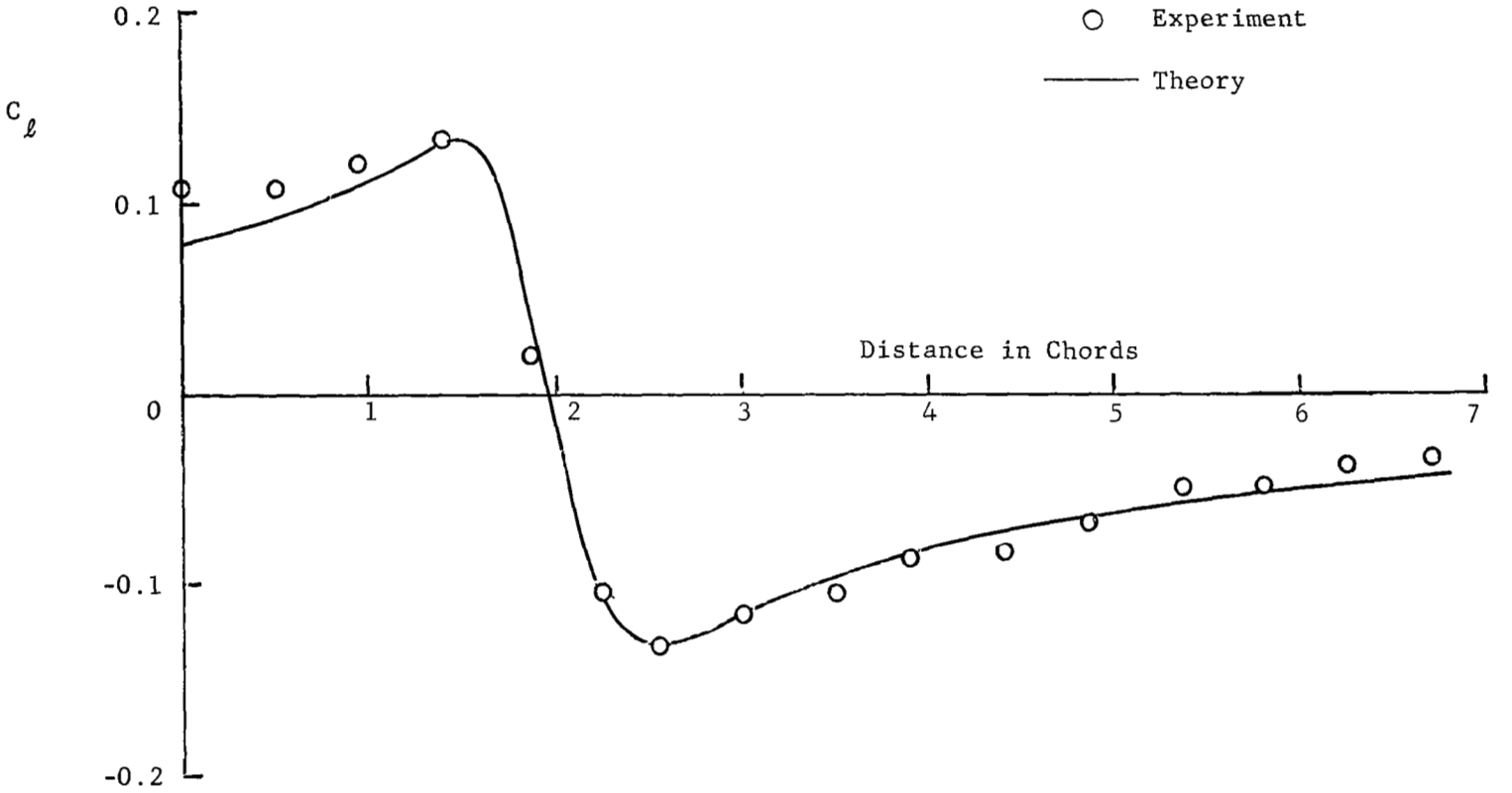

Fig. 23c Section Lift Coefficient Variation Through the Vortex; h/c = -0.25

VI. CONCLUSIONS

Results of an experimental investigation of rotor blade-vortex interaction have been presented. The following conclusions are drawn from the results obtained at a spanwise station of 95%.

1. This investigation proves the feasibility of studying the rotor-vortex interaction effects in a wind-tunnel for well-defined vortex and rotor parameters.
2. A typical distance of 10 chord lengths, equal to approximately 65° of azimuthal travel, is needed before the vortex effects are negligible.
3. Maximum section lift coefficient differences, ΔC_{ℓ}, and their time-rate-changes always reach their maximums if the rotor penetrates the center of the vortex.
4. Values as high as 0.7 in ΔC_{ℓ} and 0.6 x 10^3/sec in $\frac{\Delta C_{\ell}}{\Delta t}$ were measured in the present experiments.
5. ΔC_{ℓ} and $\frac{\Delta C_{\ell}}{\Delta t}$ increase approximately linearly with vortex strength. The slopes of these lines are different for different rotor plane and shaft axis positions.
6. ΔC_{ℓ} increases as the shaft axis is moved away from the vortex axis (i.e. as the intersection angle, δ, decreases) due to the combined effect of increased resultant velocity and vortex dimensions as the blade experiences them. However, $\frac{\Delta C_{\ell}}{\Delta t}$ first increases

up to an intersection angle of 71.5° starting from 90° and then decreases gradually with the decrease of intersection angle.

7. A simplified quasi-steady approach predicts reasonably well the variation of $\frac{C_\ell}{C_{\ell peak}}$, but over-estimates the peak section lift coefficient as the blade passes through a vortex.

8. The rotor blades can experience as much negative lift as positive lift during their encounter with the tip vortex.

APPENDIX

BLADE LOADING

The problem of predicting the time history of the loading on a small area of the blade subjected to a gust of finite length was treated by Leverton and Taylor in reference 5. This small area of the blade was treated simply as a two-dimensional airfoil.

Approximating the gust profile to a sine wave, and representing the gust as a series of harmonics based on the gust width as the fundamental length, the amplitude of the harmonics falls off rapidly. Using this approach, the loading was given by two separate expressions, one when the blade is experiencing the gust (equation A.1) and the other when the loading decays as the blade passes out of its effect (equation A.2)

$$L_m = \frac{1}{2}\rho VC\, a_o\, W_m \left\{ \frac{0.065}{\sqrt{K_m^2 + (0.13)^2}} \left[\mathrm{Sin}\,(K_m s - \phi) + e^{-0.13s} \frac{K_m}{\sqrt{K_m^2 + (0.13)^2}} \right] + \frac{0.5}{\sqrt{K_m^2 + 1}} \left[\mathrm{Sin}(K_m s - \alpha) + e^{-s} \frac{K_m}{\sqrt{K_m^2 + 1}} \right] \right\} \tag{A.1}$$

$$L_m = \frac{1}{2}\rho VC\, a_o\, W_m \left\{ \frac{0.065\, e^{-0.13s}}{\sqrt{K_m^2 + (0.13)^2}} \left[e^{0.13x}\, \mathrm{Sin}(K_m x - \phi) + \frac{K_m}{\sqrt{K_m^2 + (0.13)^2}} \right] + \frac{0.5\, e^{-s}}{\sqrt{K_m^2 + 1}} \left[e^{x}\, \mathrm{Sin}(K_m x - \alpha) + \frac{K_m}{\sqrt{K_m^2 + 1}} \right] \right\} \tag{A.2}$$

where

m = harmonic order of gust

s = non-dimensional distance measured from beginning of gust, $\frac{Vt}{b}$

$K_m = \frac{2\pi bm}{Y}$

b = half chord = $\frac{C}{2}$

Y = total length of gust

x = non-dimensional length of gust, $\frac{Y}{b}$

$\alpha = \tan^{-1} K_m$

$\phi = \tan^{-1}(\frac{K_m}{0.13})$

The total loading can be determined by the addition of those due to individual harmonics

REFERENCES

1. Gaetano Falabella, Jr., and Meyer, J. R., Determination of Inflow Distributions from Experimental Aerodynamic Loading and Blade-Motion on a Model Helicopter Rotor in Hovering and Forward Flight. NASA TN-3492, November, 1955.

2. Hoffman, E. R., and Joubert, P. N., Turbulent Line Vortices. Journal of Fluid Mechanics, Vol. 16, Pt. 3, July, 1963 pp. 395-411.

3. Huston, R. J., Wind-Tunnel Measurements of Performance, Blade Motions and Blade Airloads for Tandem-Rotor Configurations with and without Overlap. NASA TN D-1971, October, 1963.

4. Leverton, J. W., Helicopter Noise - Blade Slap, Part 1. Review and Theoretical Study. NASA CR-1221, October, 1968.

5. Leverton, J. W., and Taylor, F. W., Helicopter Blade Slap. Journal of Sound and Vibration 4(3) pp. 345-357 (1966).

6. May, D. M., The Development of a Vortex Meter. M.S. Thesis, 1964. The Pennsylvania State University, University Park, Pennsylvania.

7. McCormick, B. W., Tangler, J. L., and Sherrieb, H. E., Structure of Trailing Vortices, AIAA J. of Aircraft, V. 5, No. 3, May-June 1968, pp. 260-267.

8. Meyer, J. R., and Gaetano Falebella, Jr., An Investigation of the Experimental Aerodynamic Loading on a Model Helicopter Rotor Blade. NASA TN-2953, May, 1953.

9. Miller, R. H., Rotor Blade Harmonic Airloading. AIAA Journal, Vol. 2, No. 3, July, 1964.

10. Miller, R. H., A Discussion of Rotor Blade Harmonic Airloading. Proc CAL/TRECOM Symposium on Dynamic Load Problems Associated with Helicopters and V/STOL Aircraft. 1963.

11. Miller, R. H., Unsteady Airloads on Helicopter Rotor Blades. Journal of Royal Aeronautical Society, Vol. 68, No. 640, April, 1964.

12. Piziali, R., Daughaday, H., and DuWaldt, F., Rotor Airloads. Proc. CAL/TRECOM Symposium on Dynamic Load Problems Associated with Helicopters and V/STOL Aircraft. 1963.

13. Pruyn, R. R., and Alexander, W. T., Jr., USAALABS Tandem Rotor Airloads Measurement Program. Journal of Aircraft, Vol. 4, No. 3, May-June, 1967.

14. Scheiman, J., and Ludi, L. H., Qualitative Evaluation of the Effect of Helicopter Rotor Blade Tip Vortex on Blade Airloads. NASA TN D-1637. 1963.

15. Simons, I. A., Some Aspects of Blade/Vortex Interaction on Helicopter Rotors in Forward Flight. Journal of Sound and Vibration, Vol. 4, pp. 268-281, November, 1966.

16. Spencer, R. H., Sternfeld, H., and McCormick, B. W., Tip Vortex Core Thickening for Application to Helicopter Rotor Noise Reduction. USAALABS TR 66-1, September, 1966.

17. Tararine, S., Experimental and Theoretical Study of Local Induced Velocities over a Rotor Disc. Proc. CAL/TRECOM Symposium on Dynamic Load Problems Associated with Helicopters and V/STOL Aircraft. 1963.

18. Willmer, M. A. P., The Loading of Helicopter Rotor Blades in Forward Flight. ARC R & M No. 3318. 1959.

NASA-Langley, 1970 — 1 CR-1573